Applied Physics Reviews

REVIEW ARTICLE | APRIL 04 2025

Metasurface biosensors: Status and prospects

Masanobu Iwanaga ✉ ; Qi Hu ; Youhong Tang

Appl. Phys. Rev. 12, 021305 (2025)
https://doi.org/10.1063/5.0253333

AIP Publishing

Applied Physics Reviews REVIEW pubs.aip.org/aip/are

Metasurface biosensors: Status and prospects

Cite as: Appl. Phys. Rev. **12**, 021305 (2025); doi: 10.1063/5.0253333
Submitted: 16 December 2024 · Accepted: 25 February 2025 ·
Published Online: 4 April 2025

Masanobu Iwanaga,[1,a)] Qi Hu,[2] and Youhong Tang[2]

AFFILIATIONS

[1]Research Centre for Electronic and Optical Materials, National Institute for Materials Science (NIMS), 1-1 Namiki, Tsukuba 305-0044, Japan
[2]Institute for NanoScale Science and Technology, Flinders University, Bedford Park, South Australia 5042, Australia

[a)]Author to whom correspondence should be addressed: iwanaga.masanobu@nims.go.jp

ABSTRACT

Metasurfaces have emerged as a rapidly evolving frontier in the fields of optics and photonics, with a growing emphasis on their potential for practical applications. The considerable volume of contributions to the study on metasurfaces has expanded, creating challenges in tracking all the advancements within this dynamic field. In this review, we select practically useful metasurfaces among the diverse metasurfaces studied so far. We refer to the selected hot research topics in metasurfaces at the beginning, succeedingly outline the status of several applications that are nearing practical applications, and then focus on biosensing applications, with particular attention to metasurface fluorescence (FL) biosensors, because FL detection is a major approach in bioscience and biotechnology. However, the contributions to FL detection by metasurface biosensors have not been reviewed in an extensive and comprehensive manner. Indeed, the metasurface FL biosensors have demonstrated capability of detecting a wide range of biomolecules including nucleic acids and proteins, such as antigens and antibodies. Notably, they offer enhanced sensitivity assays and reduced assay time when compared to conventional commercial assays. We here provide a focused review on the current status and future directions of metasurface biosensors.

TABLE OF CONTENTS

I. INTRODUCTION

Metasurfaces are attracting great interest as a cutting-edge optical and photonic technology and developing for various applications. The present growing metasurface research and development (R&D) origin in unconventional reflection using metallic metasurface with a complicated unit cell consisting of a set of different V-shaped structures.[1] The term "metasurfaces" is presumably derived from metamaterials—a research field that has been the subject of extensive investigation for nearly 20 years, dating back to 1999.[2–4] The conceptual framework of metasurfaces represents a significant departure from that of metamaterials. To realize optical functions, complicated unit cells and nonperiodic structures have been conceived and designed in metasurfaces, whereas metamaterials were characterized as uniformization of microstructured/nanostructured materials using effective optical indices, such as effective permittivity and permeability. Historically, the term "metasurfaces" already appeared in 2004,[5] yet its conceptualization was closely tied to that of metamaterials and did not catalyze diverse R&D across a wide range of optical and photonic applications.

Contemporary R&D exploiting metasurfaces are being globally conducted with huge efforts. Figure 1 presents representative metasurfaces that have been experimentally validated, showcasing their potential for practical applications, such as light wave manipulation,[1] metalenses,[6–8] infrared (IR) absorbers,[9] emitters,[10] and biosensors.[11,12]

Prior to delving into the specific applications shown in Fig. 1, we address underlying key physics involved in metasurface studies. First, plasmonic and dielectric nanostructures were individually investigated and found to exhibit pronounced optical resonances, termed Mie resonances.[13] Around the year 2000, noble metal nanoparticles were synthesized chemically in various shapes, such as spheres, triangles, and rods, and characterized as Mie resonators, owing to their strong light scattering attributed to intrinsic optical resonances.[14–16] In addition, dielectric nanostructures were are shown to function as electric dipole (ED) and magnetic dipole (MD) resonators, with theoretical analyses for ideal spherical shapes.[17] The analyses approximately account for the prominent resonances observed in various configurations of dielectric nanostructures.[18,19] Second, the concept of bound states in the continuum (BIC) in photonics was reported on a light-confined mode within a photonic crystal in 2013.[20] The photonic BIC modes are hidden in symmetric configurations, becoming observable only when asymmetry is introduced. For example, by introducing structural asymmetry in unit cell, the BIC modes can be observed even under normal incidence that is a symmetric configuration regarding optical excitation. This property stimulated extensive studies on BIC in metasurfaces,[21–28] which pursued narrow linewidth resonant modes of high-quality (Q) factors.

Rapid progress in metasurfaces is based on high-precision numerical simulations and contemporary nanolithography. Regarding the numerical simulations, finite-difference time-domain (FDTD)[29–31] finite element method (FEM)[32] and rigorous coupled-wave analysis (RCWA) method[33–35] are widely employed to design and evaluate optical properties of metasurfaces. They were already established by numerous publications on photonic crystals, metamaterials, and metasurfaces, which showed good agreement of the simulated results with experimentally measured results. In addition to independent development of the source codes for the numerical simulations, commercial FDTD, FEM, and RCWA packages are available, enabling many researchers to easily join the metasurface studies.

Let us briefly describe several topics on metasurfaces that exhibited substantial progresses since the 2010s. Initially, the topic of ray control emerged, introducing the design and fabrication of a metasurface of elaborate unit cell in 2011,[1] as shown in Fig. 1(a) (yellow); the

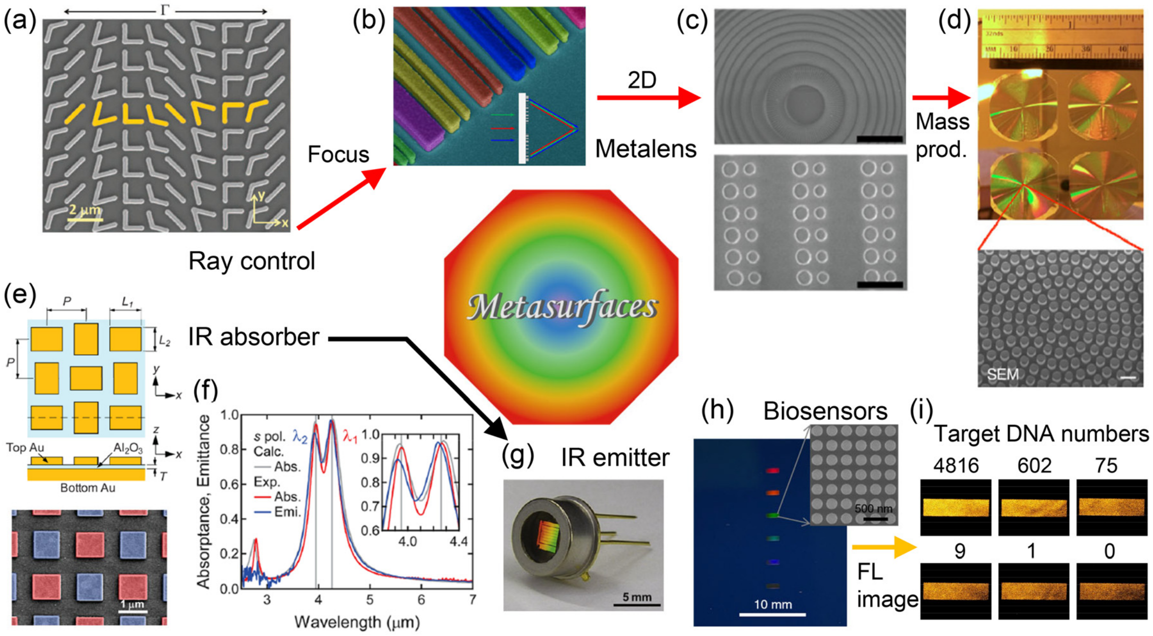

FIG. 1. Collection of representative metasurfaces for various applications. (a) Metasurface composed of a V-shaped unit cell (yellow).[1] (b) 1D metalens working at telecommunication wavelengths.[6] (c) Metalens with nearly unity numerical aperture:[7] low- and high-magnification scanning electron microscopy (SEM) images (upper and lower) with scale bars of 10 μm and 500 nm, respectively. (d) Mass productive metalenses:[8] Photograph of 2 cm diameter metalenses (upper) and SEM image with scale bar of 2 μm, magnifying the center of the metalens (lower). (e) IR absorber:[9] Design (upper) and SEM image of a fabricated sample (lower), where two different types are shown with blue and red. (f) Experimental absorptance (red) and emittance (blue) by the IR absorber.[9] (g) Photograph of a packaged IR emitter.[10] Scale bar indicates 5 mm. (h) Metasurface fluorescence (FL) biosensors.[11] (i) FL images of the metasurface biosensors employed in single cfDNA sensing.[12] Target DNA numbers per test are shown together. (a) From Yu *et al.*, Science **334**, 333 (2011). Reprinted with permission from American Association for the Advancement of Science (AAAS). (b) Adapted with permission from Khorasaninejad *et al.*, Nano Lett. **15**, 5358 (2015). Copyright 2015 American Chemical Society (ACS). (c) Adapted with permission from Paniagua-Domínguez *et al.*, Nano Lett. **18**, 2124 (2018). Copyright 2018 ACS. (d) Adapted from She *et al.*, Opt. Express **26**, 1573 (2018). (e,f) Reproduced from [Miyazaki *et al.*, Appl. Phys. Lett. **105**, 121107 (2014)] with the permission of AIP Publishing. (g) Adapted from Miyazaki *et al.*, Sci. Technol. Adv. Mater. **16**, 035005 (2015); licensed under a Creative Commons Attribution (CC BY) license. (h) Adapted from Iwanaga, Biosensors **13**, 377 (2023); licensed under a CC BY license. (i) Adapted with permission from Iwanaga *et al.*, Nano Lett. **23**, 5755 (2023). Copyright 2023 ACS.

periodicity in the horizontal was 11 μm and the working wavelength was 8 μm; the Au microstructures of 220 nm width and 50 nm height were fabricated on a Si wafer. The primary aim was to manipulate wavefront of refracted light through the design of subwavelength V-shaped structures, which reinforced a particular refraction component due to wavefront interference and traveled along one of the allowed reflective diffraction directions. This study strikingly stimulated many studies on ray and wavefront control.[36,37] As an extension of this study, phase and/or polarization control was also explored in various configurations for the visible and near infrared (IR) light,[38,39] which were often nonperiodic and non-uniform nanostructures, similar to the metalenses in Figs. 1(b) and 1(c).

Furthermore, as a natural progression of the ray and wavefront control concepts, focus effects were examined through both numerical simulations and experimental validations. The studies yielded metalenses, sometime called flat lenses.[6–8,36,40–46] Most of metalenses were designed at the height of sub micrometer, and the height was the same in each metalens. Thus, from a macroscopic view, the metalenses are characterized by their flat geometry. The principle for the focusing effect is in common with conventional convex or concave optical lenses, made of glass or quartz. The key difference is that the ray is bent in the metasurface layer of subwavelength thickness, owing to the precise alternation of the phase of light. Further improved designs led experimental demonstrations of achromatic or multiwavelength metalenses.[8,36,40–42,46]

Metalenses composed of subwavelength structures enable the integration of multifunctional units. Indeed, this capability was exploited to design color splitters,[47–49] which effectively focus the individual red, green, and blue (RGB) components of light onto separate pixels. This advancement is beneficial to produce ultracompact CMOS cameras, which will be found in smart phones and tablets soon. These optical functions of metalenses are elaborated later (Sec. II). Although the designs of the color splitters are more complex than those of metalenses, the fundamental principle for design is in common with the metalenses, which means that the color splitters belong to a family of metalenses.

Metagratings were also conceived along the concept of metasurface.[50–55] Conducting elaborate designs using computers enabled to obtain nearly 100% diffraction efficiency. The large degree of freedom in the structural designs yielded a diverse range of diffraction responses. Historically, a similar notion to the metagratings was reported in 1998,[56] where a subwavelength grating was designed and fabricated to obtain superior diffraction efficiency compared to conventional échlette gratings. The control of phase of refracted light was analyzed at the time. More elaborate and extensive designs for metagratings have significantly enriched the capabilities of subwavelength gratings.

Holography is a well-established optical technique that modulates both the amplitude and phase of light beam. Since metasurfaces can control the amplitude and phase with large degree of freedom, metasurfaces are suitable for holographic applications. Indeed, several reports experimentally showed fine holographic images using plasmonic or all-dielectric metasurfaces.[57–60] The designs of holographic metasurfaces are also elaborate tasks; however, it is implementable with help of current computational tools on personal computers.

Nonlinear effects on metasurfaces have been also extensively explored. There are two main directions: Lasing[61–63] and higher-order harmonic generation, specifically, second-order harmonic generation (SHG) and third-order harmonic generation (THG).[64–69] The studies on lasing effect primarily focused on developing ultralow-threshold lasing devices on BIC, which is a high-Q resonance and is considered to make the lasing threshold lower. In reality, a low lasing threshold at 55 μ W was observed under optical pumping.[61] Regarding the higher harmonics generations, improvement of the conversion efficiency was expected. Such an improvement has been tested frequently using plasmonic nanostructures (i.e., metallic nanostructures) from the viewpoint of local electric-field enhancement; the highest SHG conversion efficiency of plasmonic systems was reported to be 7.5×10^{-2}% at a mid-IR range.[66] However, in 2016 and 2017, more efficient SHGs were developed by exploiting dielectric nanostructures, which are Mie nanoresonators;[70–72] the dielectric was AlGaAs, which enables lower optical loss and a higher pumping threshold than the metallic nanostructures made of Au or Ag. Although optical metasurfaces optimized for SHG and THG remain unreported, the potential for designing such nonlinear metasurfaces is promising, based on efficient dielectric nanoresonators.[70–73]

Very thin, artificially engineered structures with subwavelength thickness were found to function as perfect light absorbers,[74–78] when they were designed incorporating light-harvesting metallic micro/nanostructures. The light absorption was attributed to plasmon-associated resonances. This principle has been adapted to the IR range through the fabrication of elongated periodic structures and was validated experimentally.[79–81] Recently, all-dielectric metasurfaces were reported to act as effective light absorbers,[82] in which Mie resonances are origin of the light absorption.

Furthermore, IR emitters were designed based on plasmonic resonators that comprised metal-insulator-metal (MIM) structures,[9] as depicted in the upper panel of Fig. 1(e). In this configuration, electromagnetic (EM) fields can be resonantly confined within the narrow insulating layer, which was confirmed conducting simulations and was shown to be underlying mechanism of the efficient light absorption.[79,80] Au or Ag was chosen the metallic component because they are good conductors and approximately behave as Drude metals in the IR range. The insulator was chosen from transparent dielectrics, such as Al_2O_3 or SiO_2. The MIM-based metasurface was fabricated through electron-beam (EB) lithography; a scanning-electron-microscopy (SEM) image is shown in the lower panel of Fig. 1(e), where blue and red are pseudocolors used to make the two types of MIM structures clear to the eye.[9] The MIM-based metasurface was optimized for two resonances at λ_1 and λ_2 in the mid-IR range, as shown in Fig. 1(f). The two resonant wavelengths correspond to the IR absorption of CO_2 gas and a reference.

Owing to reciprocity,[83,84] light absorptance is equivalent to emittance. Therefore, perfect light absorbers at a wavelength can work as optimal emitters at the same wavelength. The reciprocal relation was experimentally substantiated by fabricating membrane structures that kept sufficient thermal insulation.[10] Fig. 1(g) shows a packaged IR emitter that integrates the mm^2-dimension metasurface in Fig. 1(e) and is powered by dry cell batteries;[10] the scale bar indicates 5 mm.

The development of IR detectors has long history.[85,86] Metasurfaces engineered for large IR absorption have been fabricated, demonstrating high-frequency responsiveness and wavelength-selective detection,[87–89] which are elaborated in more details later (Sec. II).

Biosensors encompass a diverse range of devices sensing small molecules in environment to those sensing large biomolecules, such as DNA and antigen/antibody. Actually, many methodologies set their goals to biosensing. We here provide a concise overview of metasurface biosensors among various biosensing techniques, which are elaborated later (Sec. II). Metasurfaces often exhibit prominent optical resonances, some of which have been applied to the resonance-shift sensing of biomolecules.[90,91] Metasurface resonances at an IR range have been apply to molecular sensing to measure light absorption using a series of narrow linewidth resonances.[92] These types of metasurface sensors have been reviewed previously.[93–95] In contrast, to the best of our knowledge, metasurface fluorescence (FL) biosensors have not been reviewed so far. As is widely known, FL sensing for biomolecules is a major technique in the fields of bioscience and biotechnology,[96] because it enables to ensure specific detection of targets and to detect extremely weak signals, thanks to the development of FL-probes for biomolecules and of FL-detection methods, such as photon counting.

Complicated structures for metasurfaces stimulated motives to design novel functional nanostructures. Many trials have been reported to date, using searching methods of inverse designs,[97–100] topological optimization,[101–104] and generative algorithm.[105,106] In addition to these approaches, nonempirical structural search can explore the possibility to find functional metasurfaces.[107–109] The reports for design procedures has been already numerous and several reviews were published.[110–114]

In this review, we survey various metasurfaces developing toward practical applications in Sec. II: Light-wave manipulations in Sec. II A, metalenses in Sec. II B, IR absorbers in Sec. II C, IR emitters/detectors in Sec. II D, and biosensors in Sec. II E. Our primarily focus is on biosensor applications highlighted in Sec. III, with particular emphasis on the FL-enhancing biosensors that ensure target-specific detections, favored in contemporary biotechnology. The basic characteristics and advantages of metasurface FL biosensors are described in detail. Thereafter, the future prospects are addressed in Sec. IV.

II. METASURFACES FOR VARIOUS APPLICATIONS

Practical potential of metasurfaces are mainly two directions: (1) realization of compact optical devices and (2) highly functional optical/photonic devices. For example, the former (1) is expected to realize ultrathin lenses of sub micrometer thickness, which are now known as metalens. Although the focusing function is similar to the conventional diffraction-limited lenses, the thickness of metalenses is more than 1000-time thinner than that of the conventional achromatic lenses, which enables to compact assemble/integration of optical devices and to lead tiny cameras as one of the applications. The latter (2) is expected to go beyond the performance of conventional devices. For example, various biosensors are now commercially used; however, the capability is almost the same for more than ten years and has not reached the ultimate level, such as one molecule detection discriminating from zero molecule. Furthermore, the current high-precision biosensing techniques, called digital methods, are demanding in cost and have not been used in daily medical tests. Highly FL enhancing metasurfaces are expected to contribute to FL-detection biosensing in more practical manners.

The good candidates of metasurfaces for applications are presented in Fig. 1, being briefly described above. This section aims not to mentions the diverse research topics but to provide descriptions for practical metasurface applications in more details than Sec. I. The followings are addressed: Light-wave manipulation (Sec. II A), metalens (Sec. II B), IR absorbers (Sec. II C), IR emitters/detectors (Sec. II D), and biosensing techniques (Sec. II E) in comparison with the existing ones to understand the status of biosensors from a wide point of view.

A. Light-wave manipulation

Wavefront control employing a metasurface composed of a series of Au V-shaped microstructures[1] is visualized in Fig. 2(a). Each Au microstructure was assumed to be fabricated on a Si wafer and numerically designed to change the phase of a reflective component. Gradual changes in the shapes correspond to the changes of the phase. By strategically arranging the set of the V-shaped microstructures including the bars that look I shapes, the phase is able to be modulated from 0 to $7\pi/4$ in Fig. 2(a). Forming a periodic structure with the unit, the refraction beam in one of the reflective directions is reinforced due to the interference, manifesting itself. This is the basic mechanism of the anomalous refraction induced by the metasurface.[1] The example

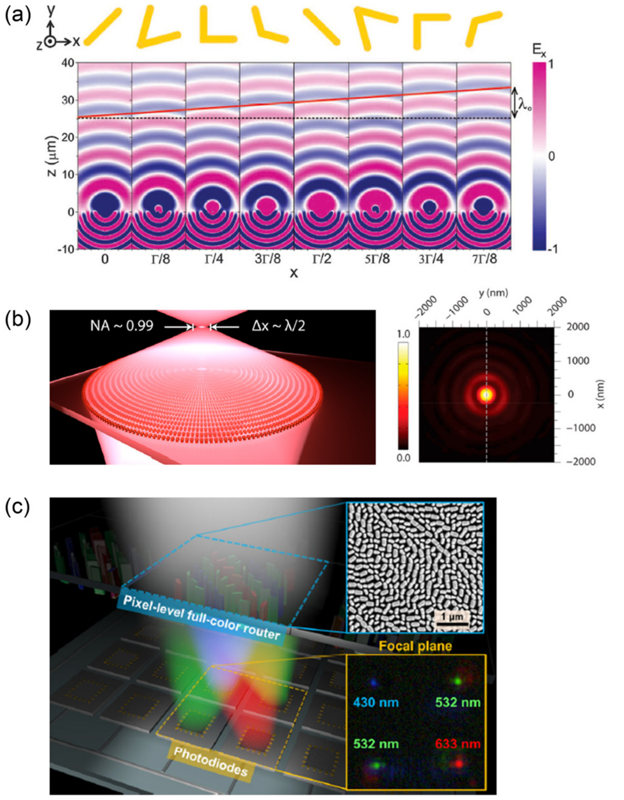

FIG. 2. Wavefront control, focusing, and color splitting by metasurfaces. (a) Wavefront modification by the V-shaped unit.[1] (b) Diffraction-limited focusing by a metalens:[7] focus image (left) and measured focal point under the diffraction limit (right). (c) Color splitting of white light into red, green, and blue (RGB) components.[48] Upper inset: SEM image of the GaN metasurface. Lower inset: measured RGB-separated focal points. (a) From Yu *et al.*, Science **334**, 333 (2011). Reprinted with permission from AAAS. (b) Adapted with permission from Paniagua-Domínguez *et al.*, Nano Lett. **18**, 2124 (2018). Copyright 2018 ACS. (c) Adapted with permission from Chen *et al.*, Nano Lett. **17**, 6345 (2017). Copyright 2017 ACS.

suggested that increasing the number of elements within the unit cell can lead to a wide range of optical responses, thereby inspiring extensive studies on metasurfaces. Early-stage contributions to the metasurface studies were collected in several review papers.[115–118]

Along the design procedures similar to those for the wavefront-manipulating metasurface in Fig. 2(a), polarization and phase control of light waves, which were often laser beams, were reported.[38,39] The fabricated subwavelength structures, i.e., metasurfaces, were often nonperiodic and nonuniform, beam and vortex shapes were modulated with a large degree of freedom.

B. Metalens

Optical focusing using a metalens is illustrated on the left side of Fig. 2(b).[7] The circular array of Si nanopillars, which are shown in Fig. 1(c), serves as a lens with a nearly unity numerical aperture (NA). The measured focal spot is shown on the right side of Fig. 2(b). This focus is diffraction-limited, meaning that the metalens functions as ordinary optical lens whereas the primarily distinction is its planar design. The height of the metalens was 250 nm and the designed array of Si nanopillars on an SiO_2 substrate formed the metasurface. The working wavelength was set at 715 nm. By adjusting the first-order diffractions in transmission and reflection components, the focal point was tuned in space. Essentially, the metalenses were designed to align with the Fresnel phase profile Φ for focusing, such that[44]

$$\Phi(x, y) = 2\pi - \frac{2\pi n}{\lambda}\left(\sqrt{x^2 + y^2 - f^2} - f\right), \tag{1}$$

where λ is the working wavelength, f is the focal length, and n is the refractive index around the unit structure of nanopillars or nanorods constituting the metalens. Equation (1) was defined on the metasurface on the xy plane. After assessing the phase change by each unit structure, the corresponding unit structures are configurated at the coordinate (x, y) in accordance with the phase determined by Eq. (1).

A more functional metalenses were explored, which are color splitters.[47–49] An example of such a color splitter is shown in Fig. 2(c).[48] White light is separated into three color components of RBG, and each separated color is focused onto different spot in a pixel of complemantary metal-oxide semiconductor camera. In other words, although the color splitter is a kind of metalens, each color component was designed to focus on a particularly designated position. Therefore, the design had more complicated than simple metalenses focusing on a in-plane position.[48] Despite this complexity, the design and fabrication were successfully executed. A GaN layer of 600 nm thickness was grown on a c-plane sapphire substrate, underwent EB-based nanolithography, and finally formed the patterned nanostructures, i.e., the color splitter; a part of it is shown in the inset of Fig. 2(c) with blue frame; the scale bar indicates 1 μm; it is seen that subwavelength multi-components working for the three colors coexist. The focusing efficiencies of the RGB components were 50.6%, 91.6%, and 87%, respectively. The focal length was 110 μm. The green component had two focal positions, as shown in the inset of Fig. 2(c) with yellow frame. It is also seen that a small crosstalk appeared at the focal positions, which could be improved by additional adjustment in designs, nanolithographic procedures, and image-processing parameters.[49]

At the end, we mention that, on the basis of these metalens R&D, metalens startup companies launched recently, aiming at the mass productive commercialization.[119,120] The compact metalenses may become available for consumer use in the near future.

C. IR absorbers

Figures 3(a) and 3(b) show snapshots of resonant EM field distributions in the MIM metasurface [Fig. 1(e)], and correspond to the resonant wavelengths λ_2 and λ_1, respectively; the xyz axes are in common in these figures. The upper panels in Figs. 3(a) and 3(b) present an electric field component, E_z, of the xy-section view in the middle of the insulator layer, and the lower panels do a magnetic field component, H_y, of the xz-section view at the position indicated with dashed lines in the upper panels. Evidently, the EM fields are strongly enhanced in the insulator layer between the metallic layers, exhibiting

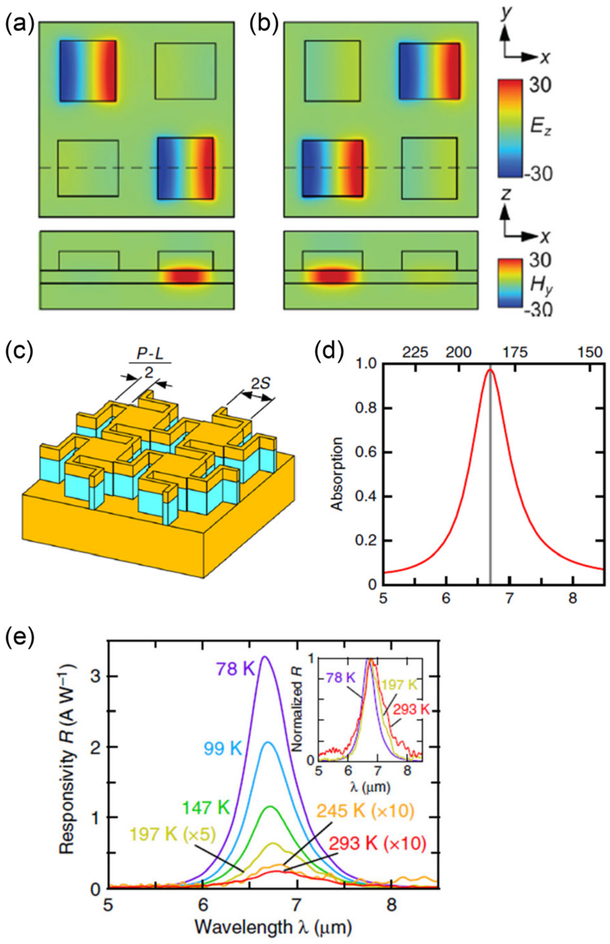

FIG. 3. IR detectors. (a) and (b) Electromagnetic (EM) distributions on large light-absorption resonance. (c) Schematic illustration of an infrared (IR) detector. The four patch cavities connected by synchronous wires. Yellow denotes Au and pale blue represents a semiconductor layer including a quantum well. (d) Simulated absorption spectrum. The horizontal axis covers a mid-IR range from 5.0 to 8.5 μm. (e) Measured responsivity spectra dependent on temperatures at 78–293 K. (a) and (b) Reproduced from [Miyazaki *et al.*, Appl. Phys. Lett. **105**, 121107 (2014)] with the permission of AIP Publishing. (c)–(e) Adapted from Miyazaki *et al.*, Nat. Commun. **11**, 565 (2020); licensed under a CC BY license.

approximately 30-fold local enhancement, relative to the incident light. This resonance is often referred to as gap plasmons. From the resonant EM field distributions, it is confirmed that the resonant modes form standing wave in the MIM structures. Note that the electric field is predominantly z-polarized when the incidence is x-polarized. This observation indicates that the incident polarization is converted to the other direction in the subwavelength MIM structures. The fundamental properties of the resonances—including the dispersion relations between wavenumber and frequency—are ascribed to coupled eigenmodes of surface plasmon polaritons in the configuration with two metal–insulator interfaces.[121–124]

Light absorbers are not restricted to only IR range. Indeed, they were explored in various artificially designed structures from microwaves to the visible range.[74–82]

D. IR emitters/detectors

Applying reciprocity to a planar object (e.g., a metasurface) at the equilibrium temperature, as drawn in Fig. 4, the Kirchhoff's law was derived in a general formalism,[83] such that

$$\alpha(\mathbf{k}, \omega) = e(-\mathbf{k}, \omega), \tag{2}$$

where $\alpha(\mathbf{k}, \omega)$ and $e(-\mathbf{k}, \omega)$ are directional light absorptance and the light emittance to the corresponding direction, respectively. The vector $\mathbf{k}$ denotes wavevector of light. Equation (2) holds at the same frequency ω. This reciprocal relation is the guide for the exploration of efficient light emitters.

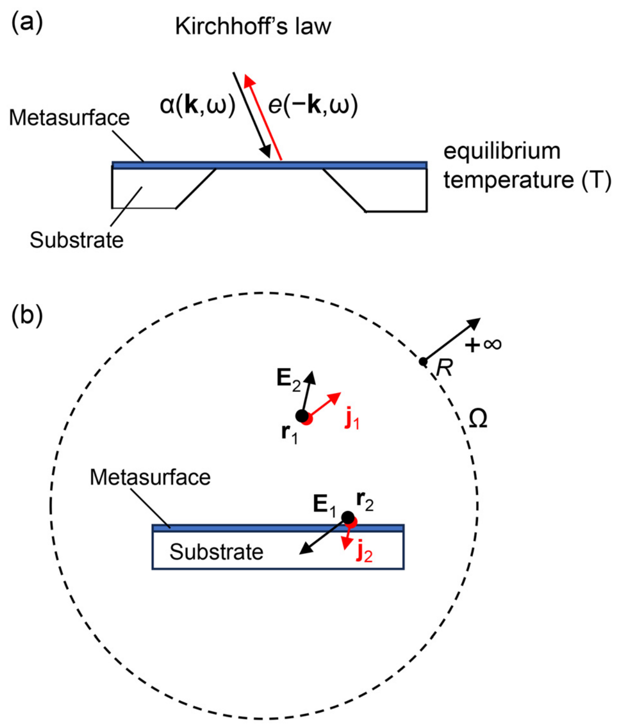

FIG. 4. Schematics of reciprocal configurations. (a) Light absorption (α) and emission (e), which is usually referred to as Kirchhoff's law [Eq. (2)]. Arrows indicate wavevectors $\mathbf{k}$ (black) and $-\mathbf{k}$ (red). (b) General configuration for Eq. (3), assuming two positions $\mathbf{r}_i$ $(i = 1, 2)$. Red arrows denote current densities $\mathbf{j}_i$. Black arrows stand for the induced electric field vectors $\mathbf{E}_i$.

With respect to the Kirchhoff's law in Eq. (2), we remark some extended configurations. The assumption to derive Eq. (2) was thermal equilibrium. If a dipole emission takes place on the metasurface at a moment, the emission minimally disturbs equilibrium because a single photon emission or a small number of photon emissions hardly change the temperature. Therefore, in the case that the emission comes from sparse dipole radiations, Eq. (2) retains its validity. This means that Eq. (2) is also a good basis for the exploration of metasurfaces with efficient FL-emission capability.

In addition to the extended application of the Kirchhoff's law, a general reciprocity holds in electromagnetics; that is, physical quantities of current density $\mathbf{j}_i$ $(i = 1, 2)$ and the induced electric field vectors $\mathbf{E}_i$ at positions $\mathbf{r}_i$ are correlated such that[125]

$$\int_{\Omega} \mathbf{j}_1(\mathbf{r}_1) \cdot \mathbf{E}_2(\mathbf{r}_1) dR = \int_{\Omega} \mathbf{j}_2(\mathbf{r}_2) \cdot \mathbf{E}_1(\mathbf{r}_2) dR, \tag{3}$$

where Ω denotes sphere with radius R. In the limit of $R \to +\infty$, Eq. (3) holds exactly. When the current density is ED, expressed as $\mathbf{p}_i \cdot \delta(\mathbf{r}_i)$, Eq. (3) is modified such as

$$\mathbf{p}_1 \cdot \mathbf{E}_2(\mathbf{r}_1) = \mathbf{p}_2 \cdot \mathbf{E}_1(\mathbf{r}_2). \tag{4}$$

Equation (4) is rewritten as $|\mathbf{E}_1|/|\mathbf{p}_1| \propto |\mathbf{E}_2|/|\mathbf{p}_2|$, which means that, when the $\mathbf{p}_1$ is the source of incident light and the $\mathbf{p}_2$ is an ED on the metasurface, the induced electric field $\mathbf{E}_1$ is proportional to the emitted field $\mathbf{E}_2$ concerning the absolute values. From this relation, we can understand that the resonant-field intensity induced by the incidence is proportional to the emitted field intensity from the metasurface. Therefore, one can assert that the FL emission from the metasurface directly correlates with the resonant fields induced by the incidence.

Generally, Eq. (4) connects an incoming wave to the reversely outgoing wave and leads reciprocity regarding transmittance and reflectance.[84,126] This is called the Helmholtz's reciprocity, which tells us that reciprocal relation holds for reflectance and transmittance.

Turning our attention to IR emitters, the reciprocal relation in Eq. (2) describes blackbody radiation and implies that perfect light absorber is simultaneously perfect light emitter. This was the principle to design and fabricate highly efficient light emitters at IR ranges.[9,10,79,80] Actually, the metasurface IR emitters tailored for CO_2 detection have been produced in a compact, packaged format, as shown in Fig. 1(g); the IR emitters consumed 31% less power than conventional thermal emitters.[9,10]

Photodetectors were readily considered as another application of metasurface IR absorbers.[87–89] The idea was akin to that for the IR emitters. However, the production of IR detectors is far more complicated than that of IR emitters, because the IR emitters go through a photon-to-photon process intrinsically in the metasurfaces, whereas the IR detectors need to transduce photon energy to electric power. The unit MIM structures need to be connected with wires, as the appearance is depicted in Fig. 3(c).[88] Thus, the IR detectors require more elaborate design and fabrication than the IR emitters. In the production of the IR detectors, a typical fabrication procedure is as follows:[88] (i) a single quantum well (QW) of semiconductor, such as n-GaAs of 4 nm, were designed through computations for electronic energy levels, especially subband levels, in the QW, in accordance with the purpose; (ii) the designed QW was grown on a wafer, such as n-

GaAs (100), together with buffer GaAs, sacrificial $Al_xGa_{1-x}As$, and contacting Si-doped layers; (iii) after electronic characterization of the growth, the set of layers of QW IR photodetector (QWIP) was coated with Ti 5 nm/Au 150 nm and bonded with another GaAs wafer; (iv) the original base wafer was removed via mechanically polishing and wet etching; (v) EB nanolithography was conducted on the wafer-removed QWIP layers, and the shapes of QWIP patches and electric wires were fabricated; (vi) Ti 5 nm and Au 150 nm layers were deposited, and then liftoff of the metallic layers were conducted; (vii) wet etching for the uncoated QWIP regions was conducted, and patch-shape QWIP and wires were obtained. Overall, the fabrication of metasurface QWIP has gone through several difficulties.

The design for the IR detector was optimized for the absorption peak at 6.7 μm. Figure 3(d) presents a simulated absorption spectra for a mid-IR range of 5.0–8.5 μm; the corresponding photon energy in meV is indicated at the top. Thus, a good design was prepared through the simulation.

The responsivity of QWIP dependent on temperature is shown in Fig. 3(e). The temperature was varied from 78 to 293 K. Obviously, the peak responsivity is located at 6.7 μm, as designed. In addition, the responsivity remains detectable even at 293 K. The temperature dependence was similar to another study on QWIP.[87] The decrease in the responsivity over 100 K was accounted for by thermal scattering of carriers. The photocurrent spectra at approximately 150 meV were hardly dependent on temperature.[87] Furthermore, heterodyne measurement showed that the metasurface QWIP is able to operate even at a high repetition of 4 GHz. The fast response is one of the advantages in the QWIP metasurfaces. Such high-repetition operations would require optimal current control, which can be realized by designing the wires for synchronous control of current.[88] To achieve better performance, quantum ratchet detector was recently reported,[89] in which the high resistance coming from potentials in multi-QW makes the thermal or background noise intrinsically smaller than that in the QWIPs.

In addition to the aforementioned wavelength-selective IR emitters and detectors, metasurface filters present a viable alternative for the development of IR detectors for gas sensing.[127] In the device incorporating the metasurface filters, other components, such as IR emitter and detectors, are chosen from conventional devices. In actual applications, this type of IR detector directly competes with the commercially available IR sensors equipped with multilayer film filters on substrates transparent to IR radiation.

E. Biosensing techniques

Biosensors represent a broad category of devices engineered for the detection of various molecules, extending beyond the domain of biomolecules. Let us start arranging the types. Table I lists biosensing techniques with respect to their working principles, target molecules, dynamic ranges in measurement, limits of detection (LODs), and robustness. In addition to commercially available techniques of surface plasmon resonance (SPR), enzyme-linked immunosorbent assay (ELISA), and polymerase chain reaction (PCR), nanostructure-based biosensing techniques are listed, such as Mie resonance, surface-enhanced IR absorption (SEIRA), electrochemical sensing, and metasurface FL biosensing.

Figure 5 shows the nanostructure-based biosensing and molecular sensing techniques, addressed in this subsection. Schematics, biosensor images, and experimental results are shown in Fig. 5: (a) SPR using Au nanoparticle (upper) and Au thin film (lower) (b) Resonance-shift metasurface biosensors based on Mie resonance, (c) BIC-based IR metasurfaces, (d) IR spectra of reference (upper) and SEIRA (lower), (e) metasurface FL biosensors detecting cfDNA, (f) metasurface FL biosensor detecting tumor

TABLE I. Comparison of biosensing techniques in terms of principle, target molecule, limit of detection (LOD), dynamic range, and robustness. Each biosensing technique is referred to, citing a representative reference. On biosensing techniques and the principles, SPR, ELISA, BIC, IR, PCR, SERS, and s-amp denotes surface plasmon resonance, enzyme-linked immunosorbent assay, bound-state in the continuum, infrared, polymerase chain reaction, surface-enhanced Raman scattering, and short-cycle amplification, respectively. A symbol of 1/0 denotes single-molecule sensing that can discriminate from zero molecules. Note that the quantities listed here are based on presented experimental data in the references, which may be different from those claimed without experimental data or sufficient statistical analysis.

Biosensing technique	Principle	Target molecule	Dynamic range	LOD	Robustness	References
SERS	enhanced Raman scattering	parathion	unshown	unshown	unshown	128
SPR	resonance shift	PSA[a]	unshown	$\sim 0.5\mu$ g/ml	unshown	129
Mie resonance	resonance shift	PSA	1–10 ng/ml	0.7 ng/ml	good	90
SEIRA	IR absorption, BIC	protein A/G	unshown	2130 molecule/μm^2	unshown	92
ELISA	enzyme reaction	CEA[b]	1.25–50 ng/ml	1.25 ng/ml	good	11
PCR	nucleic acid amplification	COVID-19	10^2–10^5 copies/test[c]	40 ± 10 copies/test	good	130
digital PCR	nucleic acid amplification	COVID-19	10–5000 copies/test[d]	10 copies/test	good	131
Electrochemical sensing	current detection	COVID-19	231–5.8×10^7 copies/μl	231 copies/μl	unshown	132
Metasurface FL sensing	enhanced FL	CEA	2–25 000 pg/ml	2 pg/ml	good	11
Metasurface FL sensing	s-amp & enhanced FL	cfDNA[e]	1–5000 copies/test[f]	1/0	good	12

[a] Prostate specific antigen, a kind of tumor markers.
[b] Carcinoembryonic antigen, a kind of tumor markers.
[c] Clinical RNA samples, 20 μl per test.
[d] 10 μl target per test.
[e] Cell-free DNA.
[f] 4 μl target solution per test.

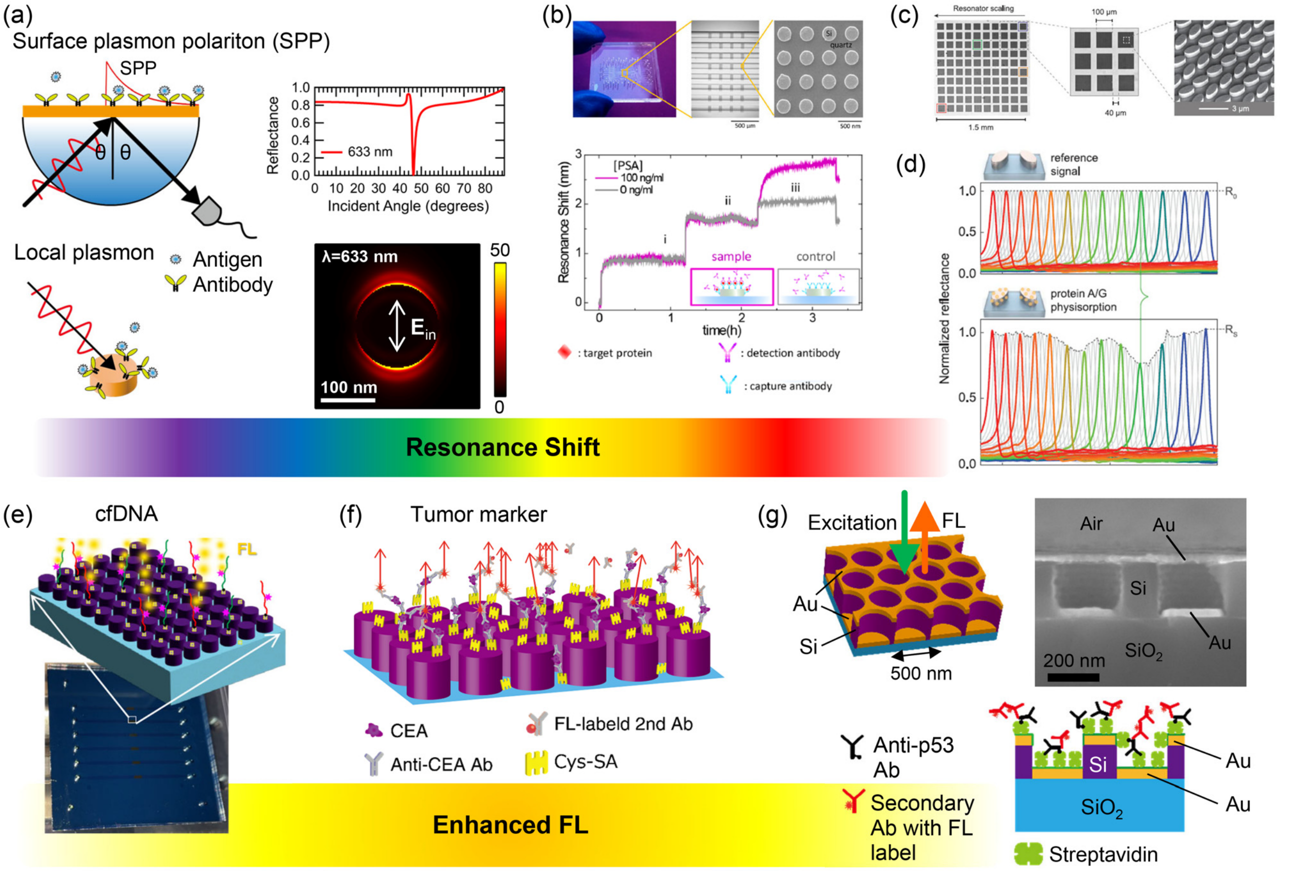

FIG. 5. Nanostructure-based biosensing and molecular sensing techniques. (a)–(d) Biosensing based on resonant wavelength shift. (a) Plasmon resonance sensing: surface plasmon polariton (SPP) configuration and reflection spectra (red curve) dependent on incident angle θ at 633 nm (upper); local plasmon induced at an Au nanostructure and resonant electric-field intensity (lower). (b) Resonance-shift-type metasurface biosensors:[90] Images of the biosensor (upper) and measured sensorgram dependent on time (lower). (c) and (d) Illustrations of BIC metasurfaces of asymmetric Si units and molecular absorption at an IR range, respectively.[92] The horizontal axes in (f) represent wavenumbers and cover the range of 1350–1800 cm^{-1}. (e)–(g) Metasurface FL biosensors, based on enhanced FL detection in common: all-dielectric ones applied for cfDNA and tumor marker CEA detections,[12,133] and plasmon-photon hybrid one,[134] respectively. (b) Adapted with permission from Yavas *et al.*, Nano Lett. **17**, 4421 (2017). Copyright 2017 ACS. (c) and (d) From Tittl *et al.*, Science **360**, 1105 (2018). Reprinted with permission from AAAS. (e) Adapted with permission from Iwanaga et *al.*, Nano Lett. **23**, 5755 (2023). Copyright 2023 ACS. (f) Adapted from Iwanaga, ACS Nano **14**, 17458 (2020); licensed under a Creative Commons Noncommercial No Derivative Works license. (g) Adapted with permission from Iwanaga, Biosens. Bioelectron. **190**, 113423 (2021). Copyright 2021 Elsevier.

marker, and (g) 3D illustration of plasmo-photonic metasurface (upper left), a section-view SEM image (upper right), and schematic of antibody detection.

1. SERS—Surface-enhanced Raman scattering

As a molecular sensing technique, surface-enhanced Raman scattering (SERS) was found in the 1970s,[135–137] was explored as an optical sensing technique since the 1980s,[138] and became popular because two appealing reports to claim single-molecule sensing were published in 1997.[139,140] In spite of the initial impact, it was found that large validation significantly reduces reproducibility.[141] This difficulty was tried to be overcome using several structures that were less dependent on so-called hot spots, which are extremely enhanced electric-field spots.[128,142,143] In spite of the appeal of the prominent SERS results, SERS has not been established as a commercial standard, probably because the reproducibility of the SERS signals has not attained. A crucial criterion for practical applications is sufficient reproducibility. SERS is kept being studied[144] after more than 20 years since the reports in 1997.

In Table I, a result of parathion molecule detection[128] is summarized. The toxic molecules were identified as a residue on the peels of fruits. The main claim was that a substantial reduction in the inhomogeneity of SERS signals was attained using densely dispersed Au nanoparticles that were coated SiO_2 shell of a few nm thickness. However, the dynamic range of the target molecules and the LOD were not shown. Therefore, it is difficult to use SERS as a quantitative method for analysis. We note that single-molecule detection has been frequently claimed in the SERS reports;[139,140] however, the concentration of the target molecule solutions typically fell within the range of micromolar (i.e., 10^{-6} mol/l); consequently, an extremely small fraction of the molecules was detected, which means that the overall detection efficiency was extremely low. To our knowledge, this issue persists to the present day.

2. SPR—Surface plasmon resonance

SPR is originally a surface plasmon polariton (SPP) excited at the flat interface of metal and dielectrics, such as air, glass, and water.[145] In a typical experimental configuration, SPP is detected using an Au thin film coupled with a prism and observed as a prominent dip at 46° in reflection spectrum (red curve) dependent on incident angle θ, as shown in Fig. 5(a) (upper). SPP is known to be sensitive to the refractive index of contacting medium and to exhibit definite resonance shift dependent on the refractive index. Therefore, resonant shift was applied for biomolecule sensing.[146] Another SPR, called local plasmons, became popular owing to the synthesis of noble-metal nanoparticles in the era of nanotechnology around 2000.[14] Local plasmons also enable the measurement of resonance shifts by immobilizing biomolecules, such as antigens and antibodies, on the surface. An illustration including an Au nanodisk is provided in Fig. 5(a) (lower). Resonant electric-field intensity of the Au nanodisk with 152 nm diameter and 80 nm height on an SiO_2 substrate, simulated using RCWA method,[124] is shown in a section view of the nanodisk, exhibiting more than 50-fold enhanced intensity than that of incident plane wave at 633 nm. The largely enhanced intensity distribution exists in 5 nm area from the outermost surface of the Au nanodisk.

In Table I, a result on prostate-specific antigen (PSA) detection[129] is listed. In an optimal condition, the PSA solution at 0.5 μg/ml was flowed and detected as a signal of 74 pg of proteins/mm^2. Although the limit of resolution for the measurement was not determined in the Ref. 129, it is presumably located at approximately 10 pg of proteins/mm^2 from the available data. Therefore, it is inferred that the LOD for PSA detection is a few fold smaller than 0.5 μg/ml but in the same order. In the same Ref. 129, cysteine-tagged protein G was detected at 2406 pg of proteins/mm^2, being equivalent to 1.03×10^5 molecules/μm^2. These results imply that the protein G was detectable by 100-fold dilution, i.e., at 1×10^3 molecules/μm^2, which is compared to a SEIRA result later (Sec. II E 5).

The SPR reports[129,146] hardly referred to robustness, which ensures selective detection of target molecules among various obstacle molecules. The SPR technique is mainly used for high-concentration target solutions and for evaluations of binding constant between particular molecules, such as antigen and the antibody. Thus, the SPR technique is not suitable for low-concentration targets but for the basic analysis within high-concentration ranges.

3. Mie resonance

Mie resonance is referred to in Sec. I. The main feature is that both metallic and dielectric nanostructures functions as optically prominent resonators.[14–19] In this sense, plasmonic or dielectric nanostructures, including metasurfaces, were readily noticed as candidates for resonance-shift biosensors.[90,91,147–151] Fig. 5(b) (upper) shows a set of images of all-dielectric metasurface biosensors composed of Si-nanodisk array. The metasurfaces and a PDMS microfluidic chip form a metasurface biosensors. A typical sensorgram is shown in Fig. 5(b) (lower).

In Table I, a result of prostate specific antigen (PSA) detection[90] is listed; PSA is a tumor marker used in daily medical diagnoses. The all-dielectric metasurfaces served as a biosensor, enabling the detection in a dynamic range of 1–10 ng/ml. The LOD was estimated to be 0.7 ng/ml. When the PSA was distributed in a human serum diluted to 50%, the detection was performed in a similar precision on the metasurfaces, yielding a dynamic range of 3–20 ng/ml and an LOD of 1.6 ng/ml, as noted in the robustness column of Table I.

4. BIC—Bound states in the continuum

A BIC is a resonance that does not show prominent optical responses under forbidden conditions. For example, a symmetry-protected BIC does not show any optical signal under the normal incidence, as noted in Sec. I. However, once the symmetry is broken by some ways, such as physical absorption of large molecules on nanostructures, a detectable optical signal appears. Further, increase in the degree of symmetry breaking gives rise to increase in the optical signal, which was often observed as resonance shift. Thus, biosensing using BIC was conducted,[22,152] in a similar manner to that using Mie resonances in Sec. II E 3.

To date, the reports on biosensing using BIC[22,152] have not been so many, compared with those using Mie resonances. The reported target was limited to exosome and detected at hundreds of femtomolar (fM, i.e., 10^{-15}mol/l). The detection level was inferior to the detection level of ~ 0.22 fM, by colorimetric techniques using Au nanoparticles.[153,154]

5. SEIRA—Surface-enhanced infrared absorption

IR absorption by molecular vibrations has been a well-known property in molecular science. Trials for SEIRA were conducted using plasmonic microstructures in the 2000s;[155,156] the metallic rods of μm length were prepared on substrates, in accordance with the IR working wavelengths. The detected molecules were self-assembled monolayer (SAM) or silk proteins, which directly contacted with the metallic microstructures. The absorption spectra were Fano shapes,[157,158] due to the interaction of the narrow linewidth resonances of molecular vibrations with the plasmonic resonance with broad linewidth. From the analyses of the experimental data, SEIRA signal enhancements ranged from 10 000- to 100 000-fold for the reference signals. The effort to improve SEIRA kept being continued, based on plasmonic structures;[159] some of the studies incorporated nanofluidic or microfluidic paths to obtain better sensing efficiency.[160–163]

In Table I, the BIC-based SEIRA using the all-dielectric metasurfaces[92] is noted. The LOD in protein detection was reported to be 2130 molecules/μm^2, which is nearly equal to 1 molecule/(2.2×2.2 nm^2). As noted in Sec. II E 2, the protein G was detected at the order of 1×10^3 molecules/μm^2 via the SPR; the in-plane density is a little smaller than the LOD evaluated by the BIC-based metasurfaces. As another comparison, the in-plane density is comparable to the densely immobilized density of proteins using a 200 μ g/ml solution, or 1 molecule/(2.24×2.24 nm^2), which was evaluated using the SPR instrument.[134] Thus, it is most likely that the BIC-based SEIRA is valid only for molecular detections at high concentrations.

SEIRA was recently measured on another BIC metasurface.[164] A thin film of polymethyl methacrylate (PMMA) of 111 nm thickness contacted with the metasurface, and the coupled systems of the PMMA and metasurface exhibited strong coupling of the BIC with a molecular vibration mode in a mid-IR range of 5.7–5.9 μm with tuning the asymmetry of the BIC metasurfaces. The interaction of the molecular vibration mode with the EM resonance in the IR range was shown to cover both weak and strong coupling regimes. Thus, BIC metasurfaces are a new platform to explore light–matter interplay.

6. ELISA—Enzyme-linked immunosorbent assay

ELISA is a commercially standard assay for proteins, such as antigen and antibody. When medical examinations for protein targets require precision, ELISAs are mostly conducted by inspection companies. Although typical detection ranges of ELISA depend on the commercial kits, they are mostly in a range of 0.5–5000 ng/ml. Although some of commercial ELISA kits claim better detection capability than the above, it is often unclear whether the capability is reproduced by users when the kits are applied to actual samples, such as serum and blood plasma.

In Table I, a result of detection for carcinoembryonic antigen (CEA), which is a kind of tumor markers, is listed. In user detections, the dynamic range was 1.25–50 ng/ml and the LOD was 1.25 ng/ml,[11] which was slightly different from the product sheet.[165] The medical criterion for CEA is 5 ng/ml. Therefore, the commercial kit showed that it serves as a diagnosis kit. It also turned out that the working range was optimized only around the medical criteron and did not guarantee high-sensitivity detection at the range of pg/ml. This result is compared with a result by the metasurface FL biosensor later (Sec. II E 10).

As a related development, great efforts were devoted to pursue a high-sensitivity assay based on the ELISA. Incorporating a fraction counting method into the conventional ELISA, digital ELISA was introduced.[166,167] At the expense of the extremely high sensitivity at pg/ml or lower, the overall cost was significantly raised in the digital ELISA. Consequently, the digital ELISA is not used for the daily medical examinations and the conventional ELISA noted above remains to be the commercial standard for protein assay.

7. PCR—Polymerase chain reaction

PCR is a standard technique for detection of nucleic acids of DNA and RNA. The amplification technique was invented in 1983 and reported in 1985.[168,169] Going through the extensive R&D, it is widely known that the PCR technique became a commercial standard for detection of nucleic acids in 1990s.

As a typical result using ordinary quantitative PCR (qPCR), Table I lists a result for COVID-19 detection.[130] As is widely recognized during the COVID-19 pandemic (2019–2022), numerous tests for COVID-19 using the qPCR were conducted worldwide. The RNA of COVID-19 was reversely transcribed to complementary DNA (cDNA), which was amplified and recorded as qPCR signals. A series of tests for actual samples showed the dynamic range of 10^2–10^5 copies/test and the LOD estimated at 40 ± 10 copies/test. The actual samples were swabs of patients and uninfected persons, and contained various obstacle molecules in reality. The detection through the reverse transcription and qPCR is robust in the practical tests. In the era of COVID-19, many trials to detect the RNA of COVID-19 were reported. Nevertheless, the qPCR was kept being the standard because the era was short and it took time for the new methods to be established in society. For providing against the future pandemic, useful new methods seem to establish their practical performance and values in advance.

Throughout the COVID-19 pandemic, numerous contributions were published and several review papers were already published.[170–175] Readers seeking further in-depth insights can consult the review literature. Regarding the COVID-19 detection, a comparison of the qPCR with the metasurface FL biosensors is discussed later (Sec. III C).

8. Digital PCR

Digital PCR (dPCR) is an improved technique of the ordinary PCR, i.e., qPCR.[176–178] The incorporation of a fraction counting method minimized background noise, thereby enhancing the precision and lowering the LOD. In reality, the LOD was improved, at most, by one order. Instead of the higher detection capability, the measurement required elaborate statistic analysis and became complicated. The instrument itself also became complicated, requiring higher cost than that for qPCR. Consequently, the dPCR is not used for the daily medical diagnoses.

As a typical result using the dPCR, a result of COVID-10 detection employing droplet dPCR[131] is listed in Table I. In comparison with the result of qPCR in Sec. II E 7, the detected signals at 10 copies/test was observed with an improved statistical confidence. The LOD was 10 copies/test. Although LOD of 5 copies/test was claimed,[131] the data of 10 and 5 copies/test overlapped with each other within one σ (σ: standard deviation), thereby being statistically indistinguishable. Generally, it is difficult to state how much the dPCR was improved for the qPCR because the process including reagents and data acquisition are different. However, fivefold–tenfold better LOD is often obtained in the dPCR. Therefore, the dPCR is currently ranked at a gold standard in the techniques for nucleic-acid detection, while it is demanding in cost.

9. Electrochemical sensor

In parallel to the biosensing techniques addressed above, electrochemical sensors have been extensively studied for various targets from gas to biomolecules. The studies are conducted more numerously than those on optical sensors, probably because the measurement is implemented by use only of current and voltage meters. Since the electrochemical sensors were reviewed frequently,[179] we here specify only the status of biosensing. A key element in electrochemical biosensing is magnetic beads that collect antibodies efficiently.[180,181] Although wide dynamic ranges for target concentrations were often claimed, they tend to be exaggerated;[182–186] indeed, the dynamic range and LOD were claimed without data or beyond the statistical limit. The electrochemical signals were heavily reduced by abundant obstacle molecules in human serums.[182,184] Thus, it is not easy to find quantitatively reliable references concerning the electrochemical biosensing.

In Table I, an electrochemical result of detection of COVID-19 RNA is listed.[132] In the experimental configuration, the RNA of COVID-19 was first extracted in viral; second, the extracted RNAs of COVID-19 were directly placed on an Au-nanoparticle-dispersed graphene; third, single-strand DNAs (ssDNAs) were added and incubated, which combined with the Au nanoparticles and served as probe for the RNAs; finally, RNAs hybridized with the ssDNA probes output electric signals. Thus, the electrochemical signals of the RNAs were detected, which were voltages and presented for the RNA concentrations of 231–5.8×10^7 copies/μl. When the concentration was 231 copies/μl, the voltage signal was substantially zero. However, the LOD was claimed to be 6.9 copies/μl,[132] which is an inconsistent, unconvincing jump from the measured data, because any justification is not provided. Therefore, the LOD is noted as 231 copies/μl in Table I. From the comparison with the qPCR and dPCR, which are amplification-based techniques, it is reasonable that the electrochemical sensing is ranked as a technique, at least, one-order less sensitive than the qPCR.

10. Metasurface FL biosensor

Images (specifically, a photograph and a micrograph) and the FL images of the all-dielectric metasurface FL biosensors are shown in Figs. 1(h) and 1(i), respectively. The biosensing images for cell-free DNA (cfDNA) and tumor-marker protein are illustrated in Figs. 5(e) and 5(f), respectively. The FL-detection biosensors based on the all-dielectric metasurfaces were validated, based on the finding of outstanding FL-enhancing capability.[187] A few years before the report,[187] plasmon-photon hybrid metasurfaces demonstrated an exceptional and highly uniform FL enhancement exceeding 2600-fold.[188,189] The underlying mechanism responsible for this prominent FL enhancement is detailed later (Sec. III).

In Table I, the results of CEA and cfDNA detection by the all-dielectric metasurface FL biosensors are listed. The CEA is a kind of tumor markers for cancers in lung, colon, and so on, and is widely used in medical diagnostics. The dynamic detection range was 2–25 000 pg/ml, which was over four-order of target concentrations, and the LOD was 2 pg/ml, which was more than 600-times lower than the LOD of 1250 pg/ml evaluated by a commercial ELISA kit,[11] as listed in Table I. In addition, the CEA detection was conducted for the CEA in human serum, and it was shown that the detection curve remained largely unaffected, indicating that the metasurface FL biosensors are robust for interfering molecules in the human serum.

Regarding the cfDNA detection by the metasurface FL biosensors, the dynamic range was 1–5000 copies/test, and the LOD was expressed using a symbol, 1/0, which means that one cfDNA was discriminated from zero. The LOD represents the ultimately high sensitivity because no better sensitivity is expected in bio- and molecular sensing. Even the dPCR has never attained this sensitivity, to our knowledge. The cfDNA detection was a combination of short-cycle DNA amplification and enhanced FL sensing, both of which are robust methods for obstacle molecules and support robust sensing for cfDNA.

11. Miscellaneous

Lateral flow technique emerges as a valuable approach for the management of liquid samples within constrained environments, thus, promoting efficient and cost-effective point-of-care biosensing solutions.[173,174,190,191] Nanostructure-based biosensors, including the metasurface biosensors, typically feature dimensions of 1 mm^2 or smaller. Therefore, they do not need to large liquid samples. Instead, it becomes important to handle small volume liquid samples, such as 50 μl. Thus, microfluidic/nanofluidic systems should be effectively incorporated with the nanostructure-based and metasurface biosensors.[90,94,160–163,192]

We mention trials for micro-/nano-optical sensors, which were surveyed from a viewpoint of miniaturization of optical sensors and efficiency improvement.[193] Metasurface optical sensors are one of the micro-/nano-sensors. In addition to the biosensing techniques addressed in this section, other candidates for circular dichroic sensors and a frequency-shift sensor were discussed.[193] Nevertheless, the concept of the micro-/nano-sensors has not been established as biosensors in terms of sensitivity, selectivity, and robustness, compared with the biosensors listed in Table I.

III. METASURFACE FL BIOSENSORS

As listed in Table I and described in Sec. II E, the metasurface FL biosensors show excellent performance among the various conventional biosensors. However, the metasurface FL biosensors have not been widely understood because they are a new type of biosensors.

In this section, we provide a comprehensive descriptions for the fundamentals of FL enhancement on the metasurfaces (Secs. III A and III B) and for the outstanding achievement using the metasurface FL biosensors, covering a diverse range of target molecules from proteins, such as antigens and antibodies, to nucleic acids, such as cfDNA and RNA-transcribed DNA (Sec. III C). Notably, an ultimate high-sensitivity was attained for the cfDNA. These were demonstrated using ordinary FL probes.

Furthermore, we address a new approach integrating the metasurface FL biosensors with functional FL probes, called aggregation-induced emission (AIE) molecules, for detection of human serum albumin (HSA) in noninvasive liquid biopsy (Sec. III D). The AIE molecules are shown to function as a new kind of FL sources on the metasurface FL biosensors, expanding the use cases toward practical biopsy.

A. Outstanding FL enhancement

The pursuit of enhanced FL intensity has been an interesting issue across the fields of optical physics and photochemistry. Since the 1980s,[203] plasmonic resonances induced at metallic nanostructures, especially nanogaps, were a plausible candidate for achieving this enhancement.[204,205] Further numerous studies were stimulated after the effective synthesis of metallic nanoparticles.[14]

A nanogap between Au bowtie-shaped nanoantennas exhibited a prominent FL enhancement in 2009;[194] the pairs of nanoantennas were fabricated through EB-based nanolithography and aligned precisely, which was different from the chemically synthesized nanoparticles. The nanogap structures shown in Fig. 6 was a realization of idea for FL enhancement on a plasmonic resonance, being favored widely. However, nanogap structures had a definite drawback, i.e., inhomogeneous FL enhancement, which was evident from the structure and the resonant EM field distribution called hotspot. While the strong FL enhancement was attained only at the nanogap, it was not observed at the nearly 99% area surrounding the nanogap. Starting from this result, we delve into the outstanding FL enhancement in this subsection.

Regarding FL-intensity enhancement, the top ten experimental results,[187–189,194–200] which reported FL-intensity enhancement factor (EF) exceeding 1000-fold, are shown in Fig. 6; the horizontal axis represents the EF in a logarithmic scale. The EF is defined as ratio of the FL intensity measured on the metasurfaces (or nanostructures) to that on a relevant reference (or flat glass or Si wafer) that does not have any enhancing effect. FL enhancement was reported in numerous reports, and it is unrealistic for us to refer to all the them that presumably exceed one thousand reports; instead, we here focus only on the top 10 results. We notice that some other references, which are not cited here, claimed over 1000-fold FL enhancement and note that the reports with substantial experimental data are selectively cited. Also, we note

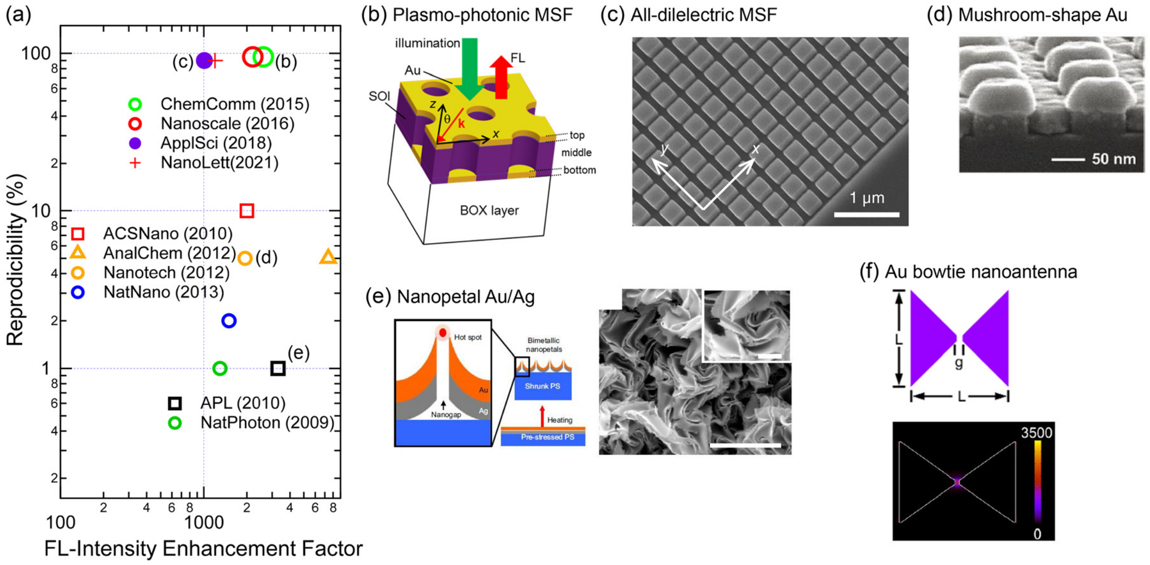

FIG. 6. Top 10 FL enhancement on metasurfaces and other nanostructures. (a) Plot of the FL enhancement for enhancement factor (EF) and reproducibility. Marks indicate data taken from literature.[187–189,194–200] Labels (b)–(f) correspond to the followings. (b) Illustration of plasmo-photonic metasurface.[201] (c) SEM image of the all-dielectric metasurface comprising an array of Si nanocolumns.[187] (d) SEM image of mushroom-shaped Au nanostructures.[198] Scale bar indicates 50 nm. (e) Nanopetal Au/Ag nanostructures:[196] schematic (left) and SEM images with a scale bar of 10 μm (right), whose inset magnifies the structure with a scale bar of 2 μm. (f) Au bowtie nanoanntena:[202] illustration for the unit (top) and simulated resonant electric fields (bottom). (b) Adapted from Iwanaga *et al.*, J. Nanomater. **2015**, 507656 (2015); licensed under a CC BY license. (c) Adapted from Iwanaga, Appl. Sci. **8**, 1328 (2018); licensed under a CC BY license. (d) Adapted with permission from Zhou *et al.*, Anal. Chem. **84**, 4489 (2012). Copyright 2012 ACS. (e) Reproduced from [Fu *et al.*, Appl. Phys. Lett. **97**, 203101 (2010)] with the permission of AIP Publishing. (f) Adapted from Sederberg and Elezzabi Opt. Express **19**, 10456 (2011).

that the cited results in Fig. 6 are limited to experimental data, and do not include purely theoretical claims or expectations based on simulations.

In Fig. 6(a), the vertical axis represents reproducibility in %, which means the percentage to observe the best EF. For instance, 50% denotes that the best EF is observed by 50% in experiment; in other words, 100 measurements result in 50 results showing the best EF and 50 results differ from the best EF, implying substantial an inhomogeneous FL-enhancement effect. We estimated the reproducibility based on the available data. The reproducibility is crucial when the enhanced FL is applied to FL sensing, because, in general, low reproducibility methods cannot deserve practical applications. We point out that the nanostructures featuring nanogaps or nanoridges exhibited low reproducibility. As far as we surveyed the related references, tens of reports showed 100- to 999-fold FL enhancement, and the other mass of reports, presumably over 500, addressed 1- to 99-fold FL enhancement. Thus, the top 10 results are exceptional; moreover, among them, the highly reproducible metasurfaces are limited only to the plasmo-photonic metasurfaces[188,189] and the all-dielectric metasurfaces of Si nanocolumn array.[187,200]

A 3D-view illustration of a plasmo-photonic metasurface is provided in Fig. 6(b). The structure includes complementary stacked Au nanostructures; there is a perforated Au film at the top and Au disks are located at the bottom; the top and bottom layers are complementary in structure to each other. Experimentally, the stacked complementary structures were formed by a normal deposition of Au. The middle layer is perforated Si slab, which is a photonic crystal. Thus, plasmonic resonances at the top and bottom layers couple with each other via photonic modes in the Si photonic crystal, which have huge photonic density of states. This unique coupled system form the plasmon-photon hybrid eigenmodes, some of which exhibit large light absorption.[206] This plasmo-photonic metasurfaces do not rely on so-called nanogaps; instead, it exhibits a macroscopic feature of large light emittance, equivalent to the large light absorption.

The plasmo-photonic metasurfaces in Fig. 6(b) were tested as a platform for FL enhancement. After a few trials and improvements, effects of excellent FL enhancement of 2600-fold at the maximum were attained.[188,189] Not only the prominent EF but also high reproducibility was obtained, which was not realized in any other platforms. The underlying mechanism is specified later (Sec. III B).

An SEM image of an all-dielectric metasurface consisting of Si nanocolumn array[187] is shown in Fig. 6(c). Whtie scale bar indicates 1 μm. The Si nanocolumns are rectangular shapes; the widths along the x and y axes are 220 nm, and the height is 200 nm. The periodicity of the array is 330 nm along the x and y axes. The metasurface was fabricated using a silicon-on-insulator (SOI) wafer. The FL enhancement corresponds to the closed purple circle in Fig. 6(a), exceeding 1000-fold. We note that the FL-enhancing capability is similar to the metasurface of circular Si-nanocolumn array. The key for the prominent FL enhancement is a higher-order magnetic resonance, specified later (Sec. III B). Both rectangular and circular Si nanocolumns have the magnetic resonance.

Another SEM image of mushroom-shaped Au structures is shown in Fig. 6(d), which was formed by Au deposition on an SiO_2

nanopillar array of 300 nm periodicity. The Au was located on the top and around the nanopillars. The strongest electric fields were identified to appear around the nanopillars because Au nanodots were formed in the deposition process. The FL EF was evaluated to be approximately 2000-fold whereas the EF was not uniform; accordingly, the reproducibility in Fig. 6(a) is estimated to be 5% from the shown experimental data. The mushroom structure is in common with that shown with an open orange triangle in Fig. 6(a). The same structure was applied to SERS measurement, and prominent Raman-scattering enhancement was reported,[142] as referred to in Sec. II E 1.

Figure 6(e) shows a schematic of nanopetal structures of Au/Ag (left) and the SEM images (right). The nanopetal structures were formed by heating of prestressed polystyrene (PS). The production process is lithography-free and a kind of bottom-up approach, while the nanogaps of Au/Ag are not controllable. The hot spots inducing locally strong electric fields are restricted to a small portion in the unit area estimated to the order of 1%. Consequently, the FL enhancement exhibits significant inhomogeneity. Considering these points, the reproducibility was assessed at 1%, shown with an open black rectangular in Fig. 6(a).

Au bowtie antenna is shown in Fig. 6(f):[202] a schematic (top) and simulated resonant electric field distribution with an indicator (bottom). In the case of gap $g = 30$ and length $L = 475$ nm, the simulations showed that the locally enhanced electric-field intensity reached 3500 at the maximum for the input of unity. Nanogap structures, such as the bowtie antenna, are widely favored in plasmonics, probably because the feature to enhance electric fields looks comprehensive for many researchers. FL molecules were dispersed around the bowtie antennas and the FL was measured. Obviously, the probability for the molecules to be at the center of the bowtie antenna (i.e., hotspot) is inevitably small. Therefore, the most enhanced FL signals are obtained, only when the FL molecules are located at the nanogap with a small probability. From the available measured data,[194] the reproducibility is estimated to be 1%, as shown with open green circle in Fig. 6(a).

Although the other structures in the top ten results are not shown in Fig. 6(a), they are similar to the structures that appears in this review. As shown with an open red square in Fig. 6(a), a MIM structure was reported to show 2000-fold FL enhancement;[195] the hot spots were sparsely dispersed; therefore, the reproducibility was approximately 10% from the measured data. Another Au bowtie antenna was reported to show over 1000-fold EF together with approximately 2% reproducible data.[199] Lately, an all-dielectric metasurface of an array of Si nanopellets with 50 nm height was reported as a platform with 1200-fold EF,[200] which is structurally similar to the all-dielectric metasurface in Fig. 6(c), except for the low height and the unit cell comprised the four elements.

Among the top ten results, the plasmo-photonic metasurfaces and the all-dielectric metasurface of Si nanocolumn array are highly reproducible, and therefore, are good candidates for practical FL biosensors. The underlying mechanism of the reproducible, high-efficiency FL enhancement is detailed in the Sec. III B.

B. Principle of FL enhancement

The whole process from photoexcitation to FL emission is illustrated in Fig. 7. This diagram depicts the outstanding FL-enhancing process on the plasmo-photonic metasurface, described in Sec. III A. Except for the energy band peculiar to the plasmo-photonic metasurface, this framework of photoexcited dynamics is in common with that on the all-dielectric metasurfaces and nanostructures in Fig. 6. In this context, the diagram is generally accountable for the FL-enhancing process.

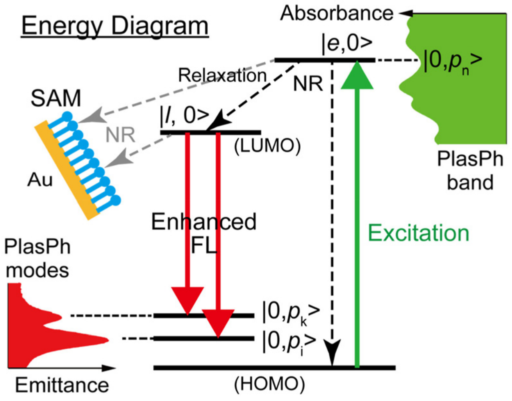

FIG. 7. Schematic of the principle of FL enhancement, describing the energy diagram involved in the FL-enhancing effect on a plasmon–photon (PlasPh) hybrid metasurface.[188] Reproduced with permission from Choi *et al.*, Chem. Commun. **51**, 11470 (2015). Copyright 2015 Royal Society of Chemistry.

The EF equation for a particular direction has been addressed frequently,[124,187,188,200,205,207,208] being phenomenologically expressed as a product of three factors as follows:

$$\mathrm{EF} = \frac{N_{\mathrm{enh}}}{N_0} \cdot \frac{\eta_{\mathrm{enh}}}{\eta_0} \cdot \frac{\gamma_{\mathrm{enh}}(\mathbf{k})}{\gamma_0(\mathbf{k})}, \tag{5}$$

where N_{enh} and N_0 denote excited populations per unit time under enhanced and reference conditions, respectively, and FL quantum yield η_i and radiative decay rate γ_i are expressed using similar subscripts to the N_i. Note that the decay rate γ depends on wavevector $\mathbf{k}$ of radiation. The ratio of $\gamma_{\mathrm{enh}}/\gamma_0$ is known as Purcell factor.[209] In Eq. (5), the Purcell factor is anisotropic and directional along the wavevector $\mathbf{k}$. Normally, the direction dependent on $\mathbf{k}$ is determined by the position of FL-signal detection. The FL quantum yield is defined such that

$$\eta = \frac{\gamma}{\gamma + \gamma_{\mathrm{NR}}}, \tag{6}$$

where γ and γ_{NR} denote radiative and nonradiative decay rates, respectively. The rates γ_{enh} and γ_0 in Eq. (5) are radiative components. Equation (6) indicates that the nonradiative decay can significantly reduce the FL yield and becomes close to 0, when $\gamma_{\mathrm{NR}} \gg \gamma$. Thus, suppression of the nonradiative rate is one of the crucial factors to attain large EF.

The ratios of N_{enh}/N_0 and $\gamma_{\mathrm{enh}}/\gamma_0$ in Eq. (5) are proportional to electric field intensity.[124] Therefore, the electric fields at the excitation and FL emission are also crucial to realize effective photoexcitation and efficient FL emission. This is the reason why various metallic and dielectric nanostructures were tested for large FL enhancement.

Another key factor is the ratio of FL quantum yield $\eta_{\mathrm{enh}}/\eta_0$. This factor is often neglected in the descriptions and analyses for FL-enhancement effects. However, it is evident that a substantial reduction of this factor significantly reduces the value of EF in Eq. (5). In the configurations that were expected to induce large FL enhancement, significant quenching of FL or photoluminescence (PL) was often observed;[141,210] such phenomena are called metal-induced quenching when metallic micro- or nanostructures are used. Not only metals but also dielectrics can induce FL or PL quenching even on the flat surface,[211] which is sometimes referred to as Föster resonant energy transfer. Thus, the excitation-state transfer to the contacting metals or dielectrics needs to be suppressed to obtain the large FL-intensity EF.

We first address the FL-enhancing mechanism on the plasmo-photonic metasurfaces in Fig. 6(b). The whole optical excitation-to-relaxation diagram is schematically illustrated in Fig. 7. Photoexcitation at 532 nm, indicated by a green arrow, corresponds to an excited state $|e,0\rangle$ of the FL molecule on the metasurface. The excitation energy is the same with that of plasmon–photon (PlasPh) hybrid mode $|0,p_\mathrm{n}\rangle$, which has large light absorptance. In reality, the mixed state of $|e,0\rangle$ and $|0,p_\mathrm{n}\rangle$ is excited, which has larger transition probability than the original $|e,0\rangle$ and enhances excitation efficiency, leading to the increase in N_enh/N_0. Following the photoexcitation, the excitation transfer takes place on an ultrafast timescale. The FL molecules located on bare Au surface could be affected by the metal-induced quenching. To avoid it, self-assembled monolayer (SAM) was introduced.[188] The SAM prevented the excited state from transferring to the Au and assisted the transition to the lowest unoccupied molecular orbital (LUMO), which is initial state of FL. Thus, the SAM contributed to the increase in the ratio η_enh/η_0. FL emission is induced via the transition from the LUMO to the highest occupied molecular orbital (HOMO) in the FL molecules. Some of the HOMO overlap in energy with the PlasPh modes of high light emittance and exhibit enhanced FL intensity. These total processes contribute to the FL EF, being expressed in Eq. (5). For the plasmo-photonic metasurfaces,[188] the experimental EF took the maximum of 2610 at 676 nm; the excitation efficiency N_enh/N_0 was estimated to be 50 from the resonant electric fields and the $\mathbf{k}$-dependent Purcell factor $\gamma_\mathrm{enh}/\gamma_0$ was experimentally determined to be 11; finally, the increase in the quantum yield η_enh/η_0 was estimated to be 47. Thus, the SAM functioned well as a block to prevent the nonradiative decay. It is crucial that the total management of the FL process led to the large EF. We stress that the large EF did not rely only on the local intense electric field enhancement, i.e., hotspot, and therefore, did exhibit high uniformity, i.e., high reproducibility.

Second, we describe the FL enhancement on the all-dielectric metasurface in Fig. 6(c). The entire process, from photoexcitation to enhanced FL emission, is similar to that in Fig. 7. The differences are that the PlasPh modes should be replaced with the resonant modes in the all-dielectric metasurface and that the SAM is unnecessary because of being free from the metal-induced quenching in the all-dielectric configuration. The design strategy for the all-dielectric metasurface to obtain the large FL enhancement was optimizing the resonance at the FL-emission wavelength.[187] When the resonances matched with the FL-emission wavelength, large FL-enhancement effects of almost 1000-fold were observed. One of the resonant modes contributing to the large FL enhancement is shown in Fig. 8. Numerically computed reflectance spectrum at the normal incidence is shown in Fig. 8(a); a red arrow indicates an FL-emission wavelength. The resonant electric- and magnetic-field distributions, $|\mathbf{E}|$ and $|\mathbf{H}|$, are presented in Figs. 8(b) and 8(c), respectively. One of the features in the resonant EM fields is that the magnetic fields are strongly localized inside the Si nanocolumn, whose boundary is drawn with white lines. The maximum of $|\mathbf{H}|$ is 11.1, compared to the incidence, meaning that the intensity $|\mathbf{H}|^2$ is 123.2 at the maximum. The multinode magnetic-field distributions indicates that the mode is a higher-order magnetic resonance. As Mie resonances, the magnetic dipole resonance has been frequently referred to.[17–19] However, the higher-order modes are rarely addressed, except for a small number of literature.[133,187] As an effect of the higher-order magnetic mode, the corresponding electric-field distributions appear on the outmost surface of Si nanocolumn, as shown in Fig. 8(b). The electric fields can contribute to the FL enhancement on the outermost surface. From the resonant electric-field distributions, the enhancement factors were estimated as follows:[187] the excitation efficiency N_enh/N_0 was approximately 20 and the FL-emission efficiency $\gamma_\mathrm{enh}(\mathbf{k})/\gamma_0(\mathbf{k})$ was approximately 50 for the total EF $= 1000$ in Eq. (5), under the assumption that the ratio of quantum yield was constant, i.e., $\eta_\mathrm{enh}/\eta_0 = 1$.

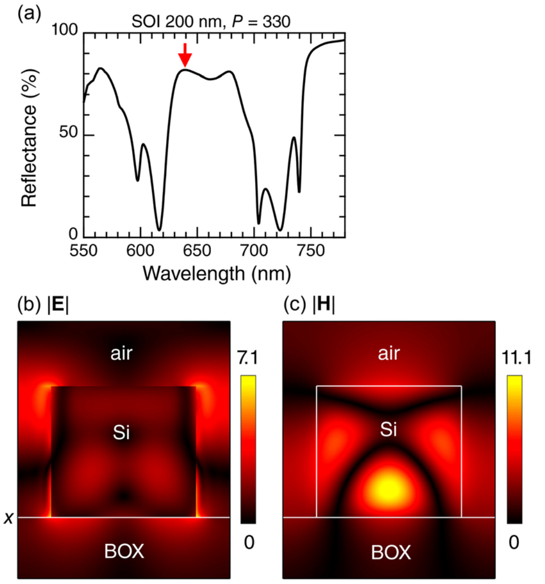

FIG. 8. FL-enhancing resonance in the all-dielectric metasurface of the Si nanocolumn array.[187] (a) Reflectance spectrum at the normal incidence. Red arrow indicates an FL-enhancing wavelength. (b) and (c) Resonant electric- and magnetic-field distributions, respectively. Adapted from Iwanaga, Appl. Sci. **8**, 1328 (2018); licensed under a CC BY license.

The principle for the EL enhancement is considered applicable for combined systems composed of the metasurfaces and other FL/PL materials. Indeed, the plasmo-photonic and all-dielectric metasurfaces in this subsection were recently tested using an atomic monolayer material of WS_2.[212,213] Regarding the PL EF, 1030- and 300-fold enhancements were observed employing the plasmo-photonic and all-dielectric metasurfaces, respectively. Thus, the framework to describe the entire photoexcitation dynamics in Fig. 7 is widely accountable for FL/PL-enhancing effects.

C. Detections with metasurface FL biosensors

In this subsection, we examine the advancements and current status of the all-dielectric metasurface FL biosensors, which are here defined as a combined pair of a metasurface substrate and a microfluidic chip made of PDMS. An appearance of the metasurface FL biosensor is seen in Fig. 5(e).

Figure 9 shows representative FL-detection results attained by the metasurface FL biosensors. The target biomolecules, detected ranges of target concentrations, and used buffers are listed in Table II. The LODs correspond to the lowest concentrations of the detection ranges. We mention that the detection ranges are potentially extended to higher concentrations.

As an antigen target, a tumor marker CEA was detected using the metasurface FL biosensors. Figure 9(a) illustrates two configurations in experiment:[11] one is a phosphate-buffer saline (PBS)-based diluent buffer suitable for proteins (left) and the other is a human serum (right). The target CEA was sandwiched using a pair of biotin-labeled and FL-labeled antibodies. Using the microfluidic paths, the metasurface FL biosensors were first coated using cysteine-tagged streptavidin (Cys-SA), and then the sandwich CEA complexes were immobilized via biotin–streptavidin coupling, which is known to be the most effective coupling between biomolecules. Thus, an effective immobilization protocol was implemented.

In Figs. 9(b) and 9(c), the results in the two configuration are shown; orange dots with error bars indicate experimental data and dashed curves represent fitted curves using the Hill equation,[216,217] which is mathematically equivalent to the four-parameter equation used widely in analysis of protein detection. The Hill equation describes immobilization reaction of the target molecules on the metasurface, being expressed as

$$y = y_0 + (S - y_0)\frac{x^n}{x^n + K_D^n}, \tag{7}$$

where y represents the FL intensity, y_0 the background level in the FL measurement, S the saturated signal intensity, x the concentration of target molecules, n the degree of cooperative reaction, and K_D the

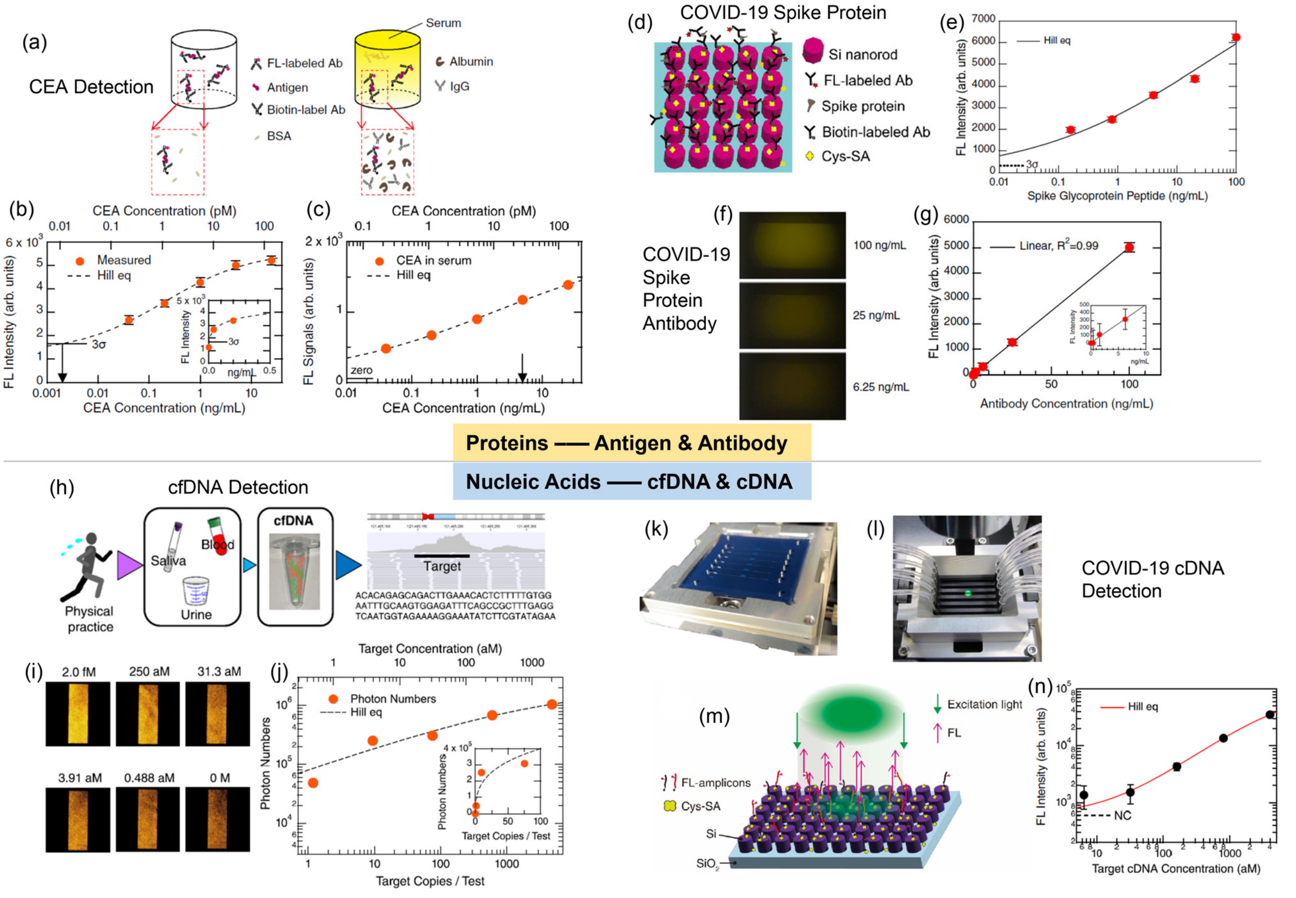

FIG. 9. Proof-of-performance of the all-dielectric metasurface FL biosensors. (a)–(c) Tumor marker CEA detection.[11] Illustrations of captured CEA in a phosphate-buffer saline (PBS) buffer with bovine serum albumin (BSA) (left) and human serum (right) are shown in (a). Detection profiles in the PBS buffer and human serum are presented in (b) and (c), respectively. Measured data are plotted with closed orange circles and dashed curves are fitted curves using the Hill equation [Eq. (7)]. (d)–(g) Detection of COVID-19 spike protein and the antibody.[214] (h)–(j) cfDNA detection.[12] A scheme from the collection of cfDNAs to the determination of the target sequence by a next-generation sequencer is shown in (h). FL images of the metasurface biosensors and the detection profile are shown in (i) and (j), respectively. (k)–(n) Detection of COVID-19 cDNA detection.[215] Photographs of the metasurface biosensors and the FL-detection configuration using a microfluidic system are shown in (k) and (l), respectively. Illustration of FL detection on the metasurface is presented in (m). The detection profile is shown in (n); closed black circles represent measured data and red curve represents the fitted profile by the Hill equation. (a)–(c) Adapted from Iwanaga, Biosensors **13**, 377 (2023); licensed under a CC BY license. (d)–(g) Adapted from Iwanaga *et al.*, Biosensors **12**, 981 (2022); licensed under a CC BY license. (h)–(j) Adapted with permission from Iwanaga *et al.*, Nano Lett. **23**, 5755 (2023). Copyright 2023 ACS. (k)–(n) Adapted from Iwanaga, Biosensors **12**, 987 (2022); licensed under a CC BY license.

TABLE II. Summary of targets detected by the all-dielectric metasurface FL biosensors. The detection range is presented, based only on the reported experimental data. SP and Ab denote spike protein and antibody, respectively.

Target	Detection range	Buffer	References
CEA	2–25 000 pg/ml	Serum	11
PSA	0.16–1000 ng/ml	Serum	11
COVID-19 SP	0.64–100 000 pg/ml	PBS + BSA	214
COVID-19 Ab	1.56–100 ng/ml	PBS + BSA	214
IgG[a]	5–2000 pg/ml	PBS + BSA	133
anti-p53 Ab	50–5000 pg/ml	PBS + BSA	133
cfDNA	0.488–2000 aM	Tris-HCl	12
COVID-19 cDNA[b]	5.86–4000 aM	Tris-HCl	215
HSA[c]	18.75–160 000 ng/ml	Urine	218

[a] Immunogloblin G.
[b] Complementary DNA.
[c] Human serum albumin.

dissociation constant of molecular interaction. The Hill equation describes a quasi-static chemical reaction, such as $A + B \to C$, which is applicable for the immobilization reaction in microfluidic paths. When we consider a simple reaction of antigen capture, the A is the antibody, the B is the antigen, and the C is the product after the reaction of A and B. The amount of reaction products is described by the Hill equation in Eq. (7).

The dynamic range of the CEA detection was 2–25 000 pg/ml, which is listed in Table I and is shown again in Table II for explicit comparison with other results using the metasurface FL biosensors. The LOD was 2 pg/ml, which was determined by evaluating the cross point of the Hill curve and 3 σ (σ: standard deviation) level from the zero concentration (i.e., negative control), as shown in Fig. 9(b). The medical criterion for CEA is 5000 pg/ml; therefore, the detection capability of the metasurface biosensors is sufficient in practice. Importantly, as shown in Figs. 9(b) and 9(c), the detection profiles were hardly affected in the case of the human serum, which has abundant obstacle biomolecules, as illustrated in Fig. 9(a). Note that the comparison with the commercially standard ELISA is already discussed in Sec. II E 10.

PSA is a widely used tumor marker for men. The detections were conducted in a similar manner to the CEA.[11] The detection range of the PSA was 0.16–1000 ng/ml, even when a buffer composed of a human serum was used, as listed in Table II. The LOD was 0.16 ng/ml, which was mainly affected by the capture and detection antibodies. As is widely known, the performance of antibodies depends on production companies; therefore, the LOD could be improved just as that of CEA. The medical criterion of PSA is now set to 4 ng/ml. Thus, the metasurface FL biosensors are practically suitable for the diagnostic purpose.

COVID-19 spike glycoproteins were detected using the metasurface FL biosensors.[214] The detection protocol was similar to that for the CEA and PSA. The configuration after immobilization on a metasurface of the Si nanocolumn array is illustrated in Fig. 9(d). Experimental data for the COVID-19 spike protein (SP) are shown with red dots with error bars in Fig. 9(e); the detection range was as wide as 0.64–100 000 pg/ml over five-order of concentrations, and the LOD was 0.64 pg/ml, evaluated based on the 3 σ level. Table II lists the quantitative results. The detection was conducted using a PBS-based diluent buffer including BSA, which is symbolically expressed as PBS+BSA in Table II.

The results concerning the detection of the antibodies against the COVID-19 spike glycoproteins are shown in Figs. 9(f) and 9(g). It was widely recognized that the antibodies functioned as a neutralizing antibody and there was a social demand to measure the concentrations in the COVID-19 pandemic. The detection configuration is similar to that in Fig. 9(d). In this case, since the target is the antibody, the spike proteins were immobilized in advance at a high concentration and the concentration-varied antibodies were detected using a FL lable.[214] Obviously, the FL images of the metasurfaces in Fig. 9(f) change the brightness in proportional to the target antibody concentrations. The FL intensities are plotted with red dots with error bars in Fig. 9(g); the inset magnifies the data near 0 ng/ml. The profile is almost linear down to 1.56 ng/ml, which was the LOD for the antibodies.

Other antibodies, such as IgG and anti-p53 antibody, were detected in ranges of pg/ml on the metasurface FL biosensors.[133] The detection procedures were similar to those for the CEA, PSA, and COVID-19 antibody. Immunoglobulin G (IgG) is the most abundant antibody in human body. The anti-p53 antibody is a tumor marker for early stage.[219–221] As listed in Table II, the detection ranges of the IgG and anti-p53 antibody were 5–2000 pg/ml and 50–5000 pg/ml, respectively, and the LODs were 5 pg/ml for the IgG and 50 pg/ml for the anti-p53 antibody. The medical criterion for the anti-p53 antibody is set to a few ng/ml. Therefore, the metasurface FL biosensors can meet the diagnostic range.

The IgG and anti-p53 antibody were also detected in the ranges of pg/ml on the plasmo-photonic metasurface biosensors.[134] The detection ranges of IgG and of anti-p53 antibody were 5–10 000 pg/ml and 50–5000 pg/ml, respectively. The detection capability was similar to that of the all-dielectric metasurface FL biosensors in Fig. 9 and Table II. From a practical and economic standpoint, the plasmo-photonic metasurfaces requires Au deposition and have a slight disadvantage, compared to the all-dielectric metasurfaces, though the FL-enhancement capability is twofold better [Fig. 6(a)].

As a nucleic acid target, cfDNA was detected, which is considered to be a next-generation diagnosis marker in the near future.[222,223] However, the concentration in liquid biopsies, such as blood, is known to be extremely low; therefore, ideally high sensitivity is required for the accurate detection. Figure 9(h) presents a schematic of cfDNA generation, collection, and sequence analysis using a next-generation sequencer;[224] the target sequence for detection was determined as displayed in Fig. 9(h). A set of the FL images on the metasurface FL biosensors is shown in Fig. 9(i), and the detection profiles are shown in Fig. 9(j)[12] where the horizontal axis represents target cfDNA concentrations in the units of copies/test and the corresponding concentrations in attomolar (aM, i.e., 10^{-18}mol/l) is indicated at the top; the inset magnifies the data near 0 copies/test, represented in linear scales. The detected signals at 1 copy/test were discriminated from 0. This demonstrates an ultimate high-sensitivity detection of DNA, which has not been realized, to the best of our knowledge, in any other biosensing techniques.

At the level of a single-target molecule, the sampling process becomes probabilistic and follows the Poisson distribution; this statistical analysis was implemented in the demonstration of the single cfDNA detection.[12] Table II lists a set of the cfDNA results, which are also referred to in Sec. II E 10. As a buffer for cfDNA, a standard buffer for DNA, Tris-HCl 10 mM, was used to conduct the short-cycle amplification procedure that suppresses falsely positive reactions and reinforces the robustness of the detection.

The COVID-19 complementary DNAs (cDNAs) were detected using the metasurface FL biosensors,[215] one of which is shown in Fig. 9(k). The FL signals were measured under illumination of green light-emitting diode (LED) light, as shown in Fig. 9(l). A schematic of FL detection of the amplicons of the COVID-19 cDNA is shown in Fig. 9(m). The experimental data (black dots with error bars) are shown in Fig. 9(n); the horizontal axis is the target concentration in aM, and the data are shown in the log-log scale. A fitted curve using the Hill equation [Eq. (7)] is shown with a red curve. As listed in Table II, the LOD was evaluated to be 5.86 aM (or 14 copies/test). Notably, this LOD was achieved through only 35 thermal cycles for nucleic-acid amplification. This LOD meets the criterion that was officially announced for reliable infection tests.[225] As we refer to in Secs. II E 7 and II E 8, typical LODs for COVID-19 were approximately 40 and 10 copies/test in the qPCR and dPCR, respectively, under the condition that the PCR cycling was conducted at more than 40 cycles, which means that more than 32-fold amplicons were produced in the qPCR and dPCR, compared to the metasurface FL biosensors. Thus, the metasurface FL biosensors exhibit a substantially better detection capability than the dPCR that is considered to be the present gold standard. Other comparisons and discussions are found in the literature.[215]

In a different approach, HSA was detected using a methodology distinct from the previously mentioned cases using the ordinary FL probes. For HSA, specific fluorogen molecules inducing AIE were incorporated. Further details are described in the Sec. III D.

D. AIE—Aggregation-induced emission

AIE is a unique optical phenomenon that molecules exhibit bright FL in their aggregated state, whereas they exhibit weak or negligible FL in their dispersed state.[227] The restriction of intramolecular motion (RIM) is currently the most widespread and accepted mechanism to explain the AIE phenomena,[228] as illustrated in Fig. 10(a). The molecular rotors, such as rotatable aromatic rings, in AIE molecules persistently consume energy from the excited state when they are completely dissolved in benign solvents, thereby leading to a fast energy decay without being released.[229] When AIE molecules aggregate, intermolecular interactions limit the spinning rotors, which causes molecules to decay through the radiation channel.[230] Based on this background, the strong hydrophobic luminous cores of AIE FL molecules are typical properties that allow them to readily form aggregates in physiological settings or aqueous media.[231] Furthermore, natural spatial restricted environment is produced by the significant steric hindrance of reactive substances especially posed by biological macromolecules, which further results in FL emission upon photoexcitation by continuous accumulation into the macromolecular structure.[232] Significantly, efficient radiative transition and photosensitization in the aggregate state promote outstanding FL emission with the characteristics of fast response, high sensitivity, "on-off" switch ability and good stability.[233]

In the past few decades, numerous researchers have successfully developed plenty of AIE FL bioprobes with high emissions and large Stroke shifts to achieve FL detection of simple and cost efficiency in biosensing.[234–237] For instance, it was reported that an AIE probe, a tetraphenylethylene (TPE) derivative sodium 1,2-bis[4–(3-sulfonatopropoxyl)phenyl]-1,2-diphenylethene (BSPOTPE) for quantitative detection of HSA.[238] This probe is non-fluorescent in PBS buffers but becomes emissive in the presence of HSA. The established FL method showed a broad linear dynamic range (LDR) of 0.0676–6.76 mg/l, LOD of 0.0676 mg/l, and an excellent selectivity to HSA. Additionally, the sensing process was also demonstrated in artificial urine, showing great potential in practical application. However, the performance of AIE probes may be interfered by autofluorescence or impurity components in actual complex biosamples.[239] Moreover, extremely low concentrations of analytes also make AIE bioprobes difficult to detect the FL signal because of the tiny amplitude of light absorption. To address those issues, a feasible expectation is to integrate AIE bioprobes into

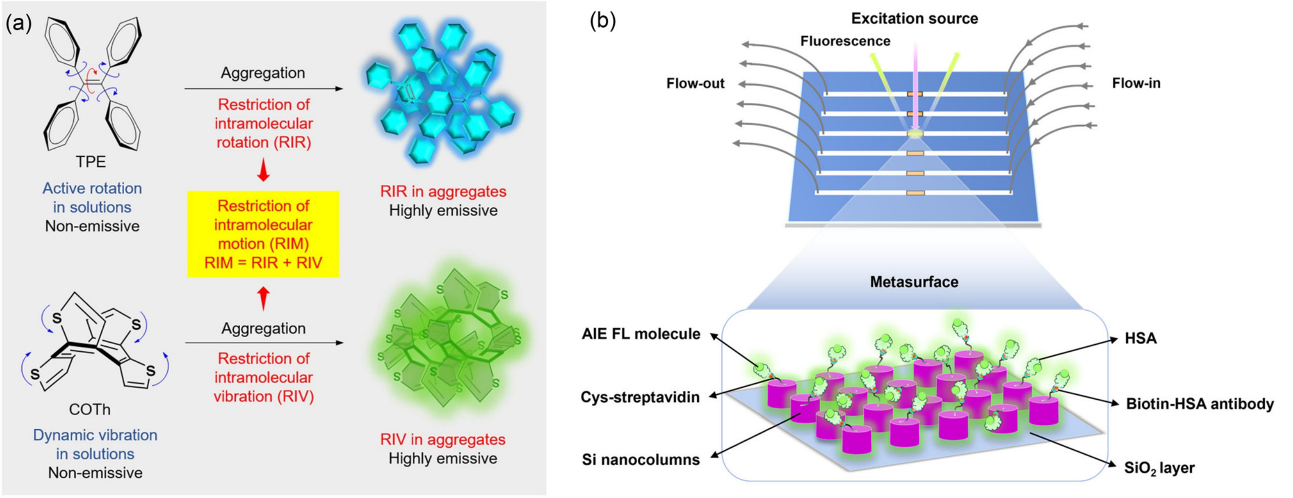

FIG. 10. (a) Mechanism of AIE phenomena.[226] (b) Schematic of AIE fluorogens incorporated with an all-dielectric metasurface FL biosensor for HSA detection.[218] (a) Adapted from Zhang *et al.*, Regen. Biomater. **10**, rbad044 (2023); licensed under a CC BY license. (b) Hu *et al.*, Adv. Opt. Mater. **12**, 2400868 (2024); licensed under a CC BY license.

compatible optical biosensors to further amplify sensitivity or reduce light loss and background noise. The all-dielectric metasurface biosensor is most likely to satisfy such requirements of AIE bioprobes.

The first study on the combination of an AIE-based fluorogen, TPE-4TA, and the all-dielectric FL metasurface FL biosensor has been conducted recently to achieve quantitative detection of trace HSA.[218] The experimental configuration is illustrated in Fig. 10(b). This metasurface FL biosensor have six independent microfluidic channels, which can be controlled to deliver different analytes simultaneously. In the meanwhile, the TPE-4TA with typical AIE characteristics can be immobilized on the metasurfaces through the flexible biofunctionalization of Si nanostructures. First, the binding molecules of Cys-SA provide a robust and durable physical adsorption layer[240] when flowing across Si nanocolumns. Second, the biotin-labeled HSA (Biotin-HSA) antibodies can establish a dense biological network via the non-covalent protein-ligand interactions between streptavidin and biotin, where HSA are captured efficiently and specifically. Third, when the tetrazolate nitrogens of TPE-4TA reacts to the polar dominant-contacting lysine residue in the HSA binding conformation through hydrogen bonding and electrostatic interactions,[241] the restriction of intramolecular motion triggers the strong FL signal.

Furthermore, the optical properties of this metasurface are suited to the excitation and emission wavelengths of the TPE-4TA.[218] The reflectance spectrum of the metasurface shows two definite reflectance bands of 30% and 70% at 360 and 530 nm, respectively. The corresponding distributions of resonant EM fields accounted for the underlying mechanism of FL enhancements.[218] The electric field distribution at 360 nm excitation wavelength predominantly appears at the upper outermost surface of Si nanocolumns, which is the most favorable zone for HSA immobilizations. This electric field distribution at the FL-emission wavelength of 530 nm qualitatively resembled with that in Fig. 8, facilitating the ED transition in the AIE molecules. The principle for the AIE enhancement is in common with that described in Sec. III B.

The FL kinetic behaviors of TPE-4TA used in the metasurface FL biosensor exhibited excellent FL stability within 2 h and a good LDR in the microalbuminuria range of 0.0188–160 μ g/ml, especially high sensitivity to the traces of HSA less than 20 μ g/ml.[218] More significantly, the FL regulation of the metasurface was superior to that of the other two conventional platforms; indeed, the metasurface FL biosensors showed a significant 25.6-fold FL enhancement for HSA detection, compared to enhancements of onefold and 3.48-fold observed in the microplate and microfluidic platforms, respectively. In the application scenarios involving human urine samples, the metasurface platform also showed the highest HSA recovery of 95.6% while the microplate and microfluidic platforms did 88.9% and 91.5% recovery, respectively. Moreover, the LOD for metasurface platform was as low as 18.75 ng/ml whereas those of microplate and microfluidic platforms were 300 and 150 ng/ml, respectively. Even when an urine sample was diluted 2560 times, the metasurface FL biosensors still possessed 10% FL retention rate of HSA. These results fully demonstrate that the metasurface FL biosensors function very efficiently for the HSA detection, which is most likely to come from the following three factors: (i) Si nanocolumns that enable HSA to immobilize is the primary factor for the effect of FL enhancement, (ii) FL amplification is determined by the local enrichment of AIE molecules, and (iii) the FL-enhancement effect of resonant EM fields. The scope of FL activities is further compressed by the spatial constraints of microfluidic pathways, while Si nanocolumns facilitate the local enrichment of FL molecules within a non-uniform stacking in a minuscule area, contributing to the FL output. Furthermore, the resonant EM fields further reinforce the FL emission of HSA and TPE-4TA conjugates, immobilized at the outermost surface of Si nanocolumns.

Summing up the HSA results, this AIE-based fluorogens incorporating with the all-dielectric metasurface FL biosensors successfully achieves FL enhancement for HSA detection. In the realistic configuration in the urine, the AIR fluorogens functioned with the metasurface FL biosensors, exhibiting high sensitivity and robustness.

IV. FUTURE PROSPECTS

In summary, we have conducted a comprehensive survey with focusing on practical applications of metasurfaces. Concretely, the metalens, metasurface IR absorber/emitter/detector, and metasurface biosensors have been addressed together with the key concepts. With a particular emphasis, the biosensing techniques are further addressed for comparison with the metasurface biosensors. Moreover, we have delineated the current status of the metasurface FL biosensors. The proof-of-concept has covered a broad range of target biomolecules across nucleic acids and proteins, such as antigens and antibodies, and has reached an ultimate sensitivity that can discriminate one target DNA from zero, which has not been attained in any other biosensors.

One of the advantages in the metasurface FL biosensors is that they are mass productive, similarly to the metalenses through high-precision, high-throughput nanolithography. Thanks to their exceptional and reproducible FL enhancement, the metasurface FL biosensors enable high-sensitivity biosensing in a simple, compact, cost-effective, and automated manner,[12] which is another practical advantage. The existing high-sensitivity methods, such as digital ELISA and digital PCR, require complicated and elaborate statistical analysis, and are demanding in cost, due to the complex instruments; these drawbacks have not been overcome for more than ten years. Considering these points, the metasurface FL biosensors are one of the good candidates for the next-generation biosensors that are applicable for diverse targets.

One of the trends in the next-generation diagnoses is to detect low-concentration targets in an aM range, such as cfDNA and microRNA. At present, the biosensing methods that can conduct a large number of short-time biosensing for the low-concentration targets have not yet been established. This is one of the most suitable issues that the metasurface FL biosensors can contribute to. As described in Sec. III, the high sensitivity, high throughput, and robustness of the metasurface FL biosensors have been substantiated for the future practical biosensing. Thus, the basic requirements for the next-generation diagnoses are satisfied.

Regarding the emerging technology, artificial intelligence (AI), it is often discussed that AI makes complicated responses by biosensors more comprehensive and feasible. However, this means that the biosensors themselves are generally hard to use and/or understand, implying that they are originally impractical. In contrast, simply speaking, the metasurface FL biosensors transduce the target biomolecule concentrations to the FL intensity, which is feasible to understand.

As one of the best scenarios in the near future, the metasurface FL biosensors will contribute to high-precision, high-throughput, and massive data-acquisition biosensing services that combine with big-data life science and data-handling AI. Although the aspect of massive data acquisition has hardly discussed regarding biosensors, one of the most significant roles of scientific devices, such as biosensors, will be to take scientifically reliable big data. This role can be efficiently conducted by the metasurface FL biosensors.[242] This role is similar to the first-principle calculations for molecular dynamics in chemistry, which yielded big data to make use of AI in the field of protein design.[243] The scientific firm ground built by quantitative biosensing data, a part of which can be acquired by the metasurface FL biosensors, will be coupled with generative AI to enable the individual to enjoy the maximized healthful life.

ACKNOWLEDGMENTS

M.I. acknowledges Takashi Hironaka, Wanida Tangkawsakul, and Saki Ishihara for their contributions to the daily measurements using metasurface FL biosensors. This study was partially supported by JSPS KAKENHI Grant Nos. JP17H01066 and JP24K01389, NIMS Priority Research Project “Biomaterials,” and Advanced Research Infrastructure for Materials and Nanotechnology (ARIM) of the Ministry of Education, Culture, Sports, Science and Technology (MEXT), Japan, Proposal No. JPMXP1223 NM5163.

AUTHOR DECLARATIONS

Conflict of Interest

The authors have no conflicts to disclose.

Author Contributions

Masanobu Iwanaga: Conceptualization (lead); Project administration (lead); Supervision (lead); Visualization (lead); Writing – original draft (lead). **Qi Hu:** Conceptualization (supporting); Validation (supporting); Writing – original draft (supporting). **Youhong Tang:** Conceptualization (supporting); Project administration (supporting); Supervision (supporting); Writing – original draft (supporting).

DATA AVAILABILITY

Data sharing is not applicable to this article as no new data were created or analyzed in this study.

REFERENCES

[1] N. Yu, P. Genevet, M. A. Kats, F. Aieta, J.-P. Tetienne, F. Capasso, and Z. Gaburro, “Light propagation with phase discontinuities: Generalized laws of reflection and refraction,” Science **334**, 333–337 (2011).
[2] J. B. Pendry, A. J. Holden, D. J. Robbins, and W. J. Stewart, “Magnetism from conductors and enhanced nonlinear phenomena,” IEEE Trans. Microwave Theory Tech. **47**, 2075–2084 (1999).
[3] J. B. Pendry, “Negative refraction makes a perfect lens,” Phys. Rev. Lett. **85**, 3966–3969 (2000).
[4] R. A. Shelby, D. R. Smith, and S. Schultz, “Experimental verification of a negative index of refraction,” Science **292**, 77–79 (2001).
[5] F. Falcone, T. Lopetegi, M. A. G. Laso, J. D. Baena, J. Bonache, M. Beruete, R. Marqués, F. Martín, and M. Sorolla, “Babinet principle applied to the design of metasurfaces and metamaterials,” Phys. Rev. Lett. **93**, 197401 (2004).
[6] M. Khorasaninejad, F. Aieta, P. Kanhaiya, M. A. Kats, P. Genevet, D. Rousso, and F. Capasso, “Achromatic metasurface lens at telecommunication wavelengths,” Nano Lett. **15**, 5358–5362 (2015).
[7] R. Paniagua-Domínguez, Y. F. Yu, E. Khaidarov, S. Choi, V. Leong, R. M. Bakker, X. Liang, Y. H. Fu, V. Valuckas, L. A. Krivitsky, and A. I. Kuznetsov, “A metalens with a near-unity numerical aperture,” Nano Lett. **18**, 2124–2132 (2018).
[8] A. She, S. Zhang, S. Shian, D. R. Clarke, and F. Capasso, “Large area metalenses: Design, characterization, and mass manufacturing,” Opt. Express **26**, 1573–1585 (2018).
[9] H. T. Miyazaki, T. Kasaya, M. Iwanaga, B. Choi, Y. Sugimoto, and K. Sakoda, “Dual-band infrared metasurface thermal emitter for CO$_2$ sensing,” Appl. Phys. Lett. **105**, 121107 (2014).
[10] H. T. Miyazaki, T. Kasaya, H. Oosato, Y. Sugimoto, B. Choi, M. Iwanaga, and K. Sakoda, “Ultraviolet-nanoimprinted packaged metasurface thermal emitters for infrared CO$_2$ sensing,” Sci. Technol. Adv. Mater. **16**, 035005 (2015).
[11] M. Iwanaga, “Robust detection of cancer markers in human serums using all-dielectric metasurface biosensors,” Biosensors **13**, 377 (2023).
[12] M. Iwanaga, T. Hironaka, N. Ikeda, T. Sugasawa, and K. Takekoshi, “Metasurface biosensors enabling single-molecule sensing of cell-free DNA,” Nano Lett. **23**, 5755–5761 (2023).
[13] G. Mie, “Beiträge zur optik trber medien, speziell kolloidaler metallösungen,” Ann. Phys. **330**, 377–445 (1908).
[14] R. Jin, Y. Cao, C. A. Mirkin, K. L. Kelly, G. C. Schatz, and J. G. Zheng, “Photoinduced conversion of silver nanospheres to nanoprisms,” Science **294**, 1901–1903 (2001).
[15] H. Kuwata, H. Tamaru, K. Esumi, and K. Miyano, “Resonant light scattering from metal nanoparticles: Practical analysis beyond Rayleigh approximation,” Appl. Phys. Lett. **83**, 4625–4627 (2003).
[16] G. Li, C. Cherqui, Y. Wu, N. W. Bigelow, P. D. Simmons, P. D. Rack, D. J. Masiello, and J. P. Camden, “Examining substrate-induced plasmon mode splitting and localization in truncated silver nanospheres with electron energy loss spectroscopy,” J. Phys. Chem. Lett. **6**, 2569–2576 (2015).
[17] R. Gomez-Medina, B. Garcia-Camara, I. Suarez-Lacalle, F. González, F. Moreno, M. Nieto-Vesperinas, and J. J. Saenz, “Electric and magnetic dipolar response of germanium nanospheres: Interference effects, scattering anisotropy, and optical forces,” J. Nanophoton. **5**, 053512 (2011).
[18] A. I. Kuznetsov, A. E. Miroshnichenko, M. L. Brongersma, Y. S. Kivshar, and B. Luk’yanchuk, “Optically resonant dielectric nanostructures,” Science **354**, aag2472 (2016).
[19] S. Kruk and Y. Kivshar, “Functional meta-optics and nanophotonics governed by Mie resonances,” ACS Photonics **4**, 2638–2649 (2017).
[20] C. W. Hsu, B. Zhen, J. Lee, S.-L. Chua, S. G. Johnson, J. D. Joannopoulos, and M. Soljačić, “Observation of trapped light within the radiation continuum,” Nature **499**, 188–191 (2013).
[21] K. Koshelev, S. Lepeshov, M. Liu, A. Bogdanov, and Y. Kivshar, “Asymmetric metasurfaces with high-Q resonances governed by bound states in the continuum,” Phys. Rev. Lett. **121**, 193903 (2018).
[22] A. Ndao, L. Hsu, W. Cai, J. Ha, J. Park, R. Contractor, Y. Lo, and B. Kanté, “Differentiating and quantifying exosome secretion from a single cell using quasi-bound states in the continuum,” Nanophotonics **9**, 1081–1086 (2020).
[23] L. Kühner, L. Sortino, R. Berté, J. Wang, H. Ren, S. A. Maier, Y. Kivshar, and A. Tittl, “Radial bound states in the continuum for polarization-invariant nanophotonics,” Nat. Commun. **13**, 4992 (2022).
[24] J. Kühne, J. Wang, T. Weber, L. Kühner, S. A. Maier, and A. Tittl, “Fabrication robustness in BIC metasurfaces,” Nanophotonics **10**, 4305–4312 (2021).
[25] H.-H. Hsiao, Y.-C. Hsu, A.-Y. Liu, J.-C. Hsieh, and Y.-H. Lin, “Ultrasensitive refractive index sensing based on the quasi-bound states in the continuum of all-dielectric metasurfaces,” Adv. Opt. Mater. **10**, 2200812 (2022).
[26] Z. Liu, T. Guo, Q. Tan, Z. Hu, Y. Sun, H. Fan, Z. Zhang, Y. Jin, and S. He, “Phase interrogation sensor based on all-dielectric BIC metasurface,” Nano Lett. **23**, 10441–10448 (2023).
[27] M. Luo, Y. Zhou, X. Zhao, Z. Guo, Y. Li, Q. Wang, J. Liu, W. Luo, Y. Shi, A. Q. Liu, and X. Wu, “High-sensitivity optical sensors empowered by quasi-bound states in the continuum in a hybrid metal–dielectric metasurface,” ACS Nano **18**, 6477–6486 (2024).
[28] T. van Loon, M. Liang, T. Delplace, B. Maes, S. Murai, P. Zijlstra, and J. G. Rivas, “Refractive index sensing using quasi-bound states in the continuum in silicon metasurfaces,” Opt. Express **32**, 14289–14299 (2024).
[29] K. S. Yee, “Numerical solution of initial boundary value problems involving Maxwell’s equations in isotropic media,” IEEE Trans. Antennas Propagat. **14**, 302–307 (1966).

[30] A. F. Oskooi, D. Roundy, M. Ibanescu, P. Bermel, J. D. Joannopoulos, and S. G. Johnson, "MEEP: A flexible free-software package for electromagnetic simulations by the FDTD method," Comput. Phys. Commun. **181**, 687–702 (2010).

[31] S. G. Rodrigo, *Optical Properties of Nanostructured Metallic Systems* (Springer, Berlin, 2012).

[32] J. L. Volakis, A. Chatterjee, and L. C. Kempel, "Review of the finite-element method for three-dimensional electromagnetic scattering," J. Opt. Soc. Am. A **11**, 1422–1433 (1994).

[33] P. Lalanne and G. M. Morris, "Highly improved convergence of the coupled-wave method for TM polarization," J. Opt. Soc. Am. A **13**, 779–784 (1996).

[34] G. Granet and B. Guizal, "Efficient implementation of the coupled-wave method for metallic lamellar gratings in TM polarization," J. Opt. Soc. Am. A **13**, 1019–1023 (1996).

[35] L. Li, "New formulation of the Fourier modal method for crossed surface-relief gratings," J. Opt. Soc. Am. A **14**, 2758–2767 (1997).

[36] D. Lin, P. Fan, E. Hasman, and M. L. Brongersma, "Dielectric gradient metasurface optical elements," Science **345**, 298–302 (2014).

[37] D. Sell, J. Yang, E. W. Wang, T. Phan, S. Doshay, and J. A. Fan, "Ultra-high-efficiency anomalous refraction with dielectric metasurfaces," ACS Photonics **5**, 2402–2407 (2018).

[38] A. Arbabi, Y. Horie, M. Bagheri, and A. Faraon, "Dielectric metasurfaces for complete control of phase and polarization with subwavelength spatial resolution and high transmission," Nat. Nanotechnol. **10**, 937–943 (2015).

[39] E. Arbabi, S. M. Kamali, A. Arbabi, and A. Faraon, "Full-stokes imaging polarimetry using dielectric metasurfaces," ACS Photonics **5**, 3132–3140 (2018).

[40] M. Khorasaninejad, W. T. Chen, R. C. Devlin, J. Oh, A. Y. Zhu, and F. Capasso, "Metalenses at visible wavelengths: Diffraction-limited focusing and subwavelength resolution imaging," Science **352**, 1190–1194 (2016).

[41] M. Khorasaninejad, Z. Shi, A. Y. Zhu, W. T. Chen, V. Sanjeev, A. Zaidi, and F. Capasso, "Achromatic metalens over 60 nm bandwidth in the visible and metalens with reverse chromatic dispersion," Nano Lett. **17**, 1819–1824 (2017).

[42] S. Wang, P. C. Wu, V.-C. Su, Y.-C. Lai, M.-K. Chen, H. Y. Kuo, B. H. Chen, Y. H. Chen, T.-T. Huang, J.-H. Wang, R.-M. Lin, C.-H. Kuan, T. Li, Z. Wang, S. Zhu, and D. P. Tsai, "A broadband achromatic metalens in the visible," Nat. Nanotechnol. **13**, 227–232 (2018).

[43] F. Callewaert, V. Velev, S. Jiang, A. V. Sahakian, P. Kumar, and K. Aydin, "Inverse-designed stretchable metalens with tunable focal distance," Appl. Phys. Lett. **112**, 091102 (2018).

[44] H. Liang, Q. Lin, X. Xie, Q. Sun, Y. Wang, L. Zhou, L. Liu, X. Yu, J. Zhou, T. F. Krauss, and J. Li, "Ultrahigh numerical aperture metalens at visible wavelengths," Nano Lett. **18**, 4460–4466 (2018).

[45] G. Brière, P. Ni, S. Héron, S. Chenot, S. Vézian, V. Brändli, B. Damilano, J.-Y. Duboz, M. Iwanaga, and P. Genevet, "An etching-free approach toward large-scale light-emitting metasurfaces," Adv. Opt. Mater. **7**, 1801271 (2019).

[46] M. D. Aiello, A. S. Backer, A. J. Sapon, J. Smits, J. D. Perreault, P. Llull, and V. M. Acosta, "Achromatic varifocal metalens for the visible spectrum," ACS Photonics **6**, 2432–2440 (2019).

[47] Y. Horie, S. Han, J.-Y. Lee, J. Kim, Y. Kim, A. Arbabi, C. Shin, L. Shi, E. Arbabi, S. M. Kamali, H.-S. Lee, S. Hwang, and A. Faraon, "Visible wavelength color filters using dielectric subwavelength gratings for backside-illuminated CMOS image sensor technologies," Nano Lett. **17**, 3159–3164 (2017).

[48] B. H. Chen, P. C. Wu, V.-C. Su, Y.-C. Lai, C. H. Chu, I. C. Lee, J.-W. Chen, Y. H. Chen, Y.-C. Lan, C.-H. Kuan, and D. P. Tsai, "GaN metalens for pixel-level full-color routing at visible light," Nano Lett. **17**, 6345–6352 (2017).

[49] M. Miyata, M. Nakajima, and T. Hashimoto, "High-sensitivity color imaging using pixel-scale color splitters based on dielectric metasurfaces," ACS Photonics **6**, 1442–1450 (2019).

[50] D. Sell, J. Yang, S. Doshay, R. Yang, and J. A. Fan, "Large-angle, multifunctional metagratings based on freeform multimode geometries," Nano Lett. **17**, 3752–3757 (2017).

[51] Z. Fan, M. R. Shcherbakov, M. Allen, J. Allen, B. Wenner, and G. Shvets, "Perfect diffraction with multiresonant bianisotropic metagratings," ACS Photonics **5**, 4303–4311 (2018).

[52] V. Neder, Y. Ra'di, A. Alù, and A. Polman, "Combined metagratings for efficient broad-angle scattering metasurface," ACS Photonics **6**, 1010–1017 (2019).

[53] H. Li, D. P. Stelling, Y. Qiu, Q. Sun, B. Chen, H. Liang, T. F. Krauss, and J. Li, "Ultra-thin transmissive crystalline silicon high-contrast grating metasurfaces," Opt. Express **27**, 30931–30940 (2019).

[54] T. Shi, Y. Wang, Z.-L. Deng, X. Ye, Z. Dai, Y. Cao, B.-O. Guan, S. Xiao, and X. Li, "All-dielectric kissing-dimer metagratings for asymmetric high diffraction," Adv. Opt. Mater. **7**, 1901389 (2019).

[55] O. Rabinovich, I. Kaplon, J. Reis, and A. Epstein, "Experimental demonstration and in-depth investigation of analytically designed anomalous reflection metagratings," Phys. Rev. B **99**, 125101 (2019).

[56] P. Lalanne, S. Astilean, P. Chavel, E. Cambril, and H. Launois, "Blazed binary subwavelength gratings with efficiencies larger than those of conventional échelette gratings," Opt. Lett. **23**, 1081–1083 (1998).

[57] X. Ni, A. V. Kildishev, and V. M. Shalaev, "Metasurface holograms for visible light," Nat. Commun. **4**, 2807 (2013).

[58] G. Zheng, H. Mühlenbernd, M. Kenney, G. Li, T. Zentgraf, and S. Zhang, "Metasurface holograms reaching 80% efficiency," Nat. Nanotechnol. **10**, 308–312 (2015).

[59] L. Wang, S. Kruk, H. Tang, T. Li, I. Kravchenko, D. N. Neshev, and Y. S. Kivshar, "Grayscale transparent metasurface holograms," Optica **3**, 1504–1505 (2016).

[60] S. M. Kamali, E. Arbabi, A. Arbabi, Y. Horie, M. Faraji-Dana, and A. Faraon, "Angle-multiplexed metasurfaces: Encoding independent wavefronts in a single metasurface under different illumination angles," Phys. Rev. X **7**, 041056 (2017).444

[61] A. Kodigala, T. Lepetit, Q. Gu, B. Bahari, Y. Fainman, and B. Kanté, "Lasing action from photonic bound states in continuum," Nature **541**, 196–199 (2017).

[62] S. T. Ha, Y. H. Fu, N. K. Emani, Z. Pan, R. M. Bakker, R. Paniagua-Domínguez, and A. I. Kuznetsov, "Directional lasing in resonant semiconductor nanoantenna arrays," Nat. Nanotechnol. **13**, 1042–1047 (2018).

[63] M.-S. Hwang, H.-C. Lee, K.-H. Kim, K.-Y. Jeong, S.-H. Kwon, K. Koshelev, Y. Kivshar, and H.-G. Park, "Ultralow-threshold laser using super-bound states in the continuum," Nat. Commun. **12**, 4135 (2021).

[64] J. Lee, M. Tymchenko, C. Argyropoulos, P.-Y. Chen, F. Lu, F. Demmerle, G. Boehm, M.-C. Amann, A. Alù, and M. A. Belkin, "Giant nonlinear response from plasmonic metasurfaces coupled to intersubband transitions," Nature **511**, 65–59 (2014).

[65] Y. Yang, W. Wang, A. Boulesbaa, I. I. Kravchenko, D. P. Briggs, A. Puretzky, D. Geohegan, and J. Valentine, "Nonlinear fano-resonant dielectric metasurfaces," Nano Lett. **15**, 7388–7393 (2015).

[66] J. Lee, N. Nookala, J. S. Gomez-Diaz, M. Tymchenko, F. Demmerle, G. Boehm, M.-C. Amann, A. Alù, and M. A. Belkin, "Ultrathin second-harmonic metasurfaces with record-high nonlinear optical response," Adv. Opt. Mater. **4**, 664–670 (2016).

[67] L. Wang, S. Kruk, K. Koshelev, I. Kravchenko, B. Luther-Davies, and Y. Kivshar, "Nonlinear wavefront control with all-dielectric metasurfaces," Nano Lett. **18**, 3978–3984 (2018).

[68] Z. Liu, Y. Xu, Y. Lin, J. Xiang, T. Feng, Q. Cao, J. Li, S. Lan, and J. Liu, "High-Q quasibound states in the continuum for nonlinear metasurfaces," Phys. Rev. Lett. **123**, 253901 (2019).

[69] C. Fang, Q. Yang, Q. Yuan, L. Gu, X. Gan, Y. Shao, Y. Liu, G. Han, and Y. Hao, "Efficient second-harmonic generation from silicon slotted nanocubes with bound states in the continuum," Laser Photonics Rev. **16**, 2100498 (2022).

[70] V. F. Gili, L. Carletti, A. Locatelli, D. Rocco, M. Finazzi, L. Ghirardini, I. Favero, C. Gomez, A. Lemaître, M. Celebrano, C. D. Angelis, and G. Leo, "Monolithic AlGaAs second-harmonic nanoantennas," Opt. Express **24**, 15965–15971 (2016).

[71] J. Cambiasso, G. Grinblat, Y. Li, A. Rakovich, E. Cortés, and S. A. Maier, "Bridging the gap between dielectric nanophotonics and the visible regime with effectively lossless gallium phosphide antennas," Nano Lett. **17**, 1219–1225 (2017).

[72] S. S. Kruk, R. Camacho-Morales, L. Xu, M. Rahmani, D. A. Smirnova, L. Wang, H. H. Tan, C. Jagadish, D. N. Neshev, and Y. S. Kivshar, "Nonlinear optical magnetism revealed by second-harmonic generation in nanoantennas," Nano Lett. **17**, 3914–3918 (2017).

[73] K. Koshelev, S. Kruk, E. Melik-Gaykazyan, J.-H. Choi, A. Bogdanov, H.-G. Park, and Y. Kivshar, "Subwavelength dielectric resonators for nonlinear nanophotonics," Science **367**, 288–292 (2020).

[74] N. I. Landy, S. Sajuyigbe, J. J. Mock, D. R. Smith, and W. J. Padilla, "Perfect metamaterial absorber," Phys. Rev. Lett. **100**, 207402 (2008).

[75] T. V. Teperik, F. J. G. de Abajo, A. G. Borisov, M. Abdelsalam, P. N. Bartlett, Y. Sugawara, and J. J. Baumberg, "Omnidirectional absorption in nanostructured metal surfaces," Nat. Photonics **2**, 299–301 (2008).

[76] P. Spinelli, M. A. Verschuuren, and A. Polman, "Broadband omnidirectional antireflection coating based on subwavelength surface Mie resonators," Nat. Commun. **3**, 692 (2012).

[77] M. Iwanaga, "Perfect light absorbers made of tungsten-ceramic membranes," Appl. Sci. **7**, 458 (2017).

[78] A. S. Rana, M. Q. Mehmood, H. Jeong, I. Kim, and J. Rho, "Tungsten-based ultrathin absorber for visible regime," Sci. Rep. **8**, 2443 (2018).

[79] J. Hendrickson, J. Guo, B. Zhang, W. Buchwald, and R. Soref, "Wideband perfect light absorber at midwave infrared using multiplexed metal structures," Opt. Lett. **37**, 371–373 (2012).

[80] P. Bouchon, C. Koechlin, F. Pardo, R. Haïdar, and J.-L. Pelouard, "Wideband omnidirectional infrared absorber with a patchwork of plasmonic nanoantennas," Opt. Lett. **37**, 1038–1040 (2012).

[81] T. D. Dao, K. Chen, S. Ishii, A. Ohi, T. Nabatame, M. Kitajima, and T. Nagao, "Infrared perfect absorbers fabricated by colloidal mask etching of Al-Al_2O_3-Al trilayers," ACS Photon. **2**, 964–970 (2015).

[82] R. Xu and J. Takahara, "All-dielectric perfect absorber based on quadrupole modes," Opt. Lett. **46**, 3596–3599 (2021).

[83] J.-J. Greffet and M. Nieto-Vesperinas, "Field theory for generalized bidirectional reflectivity: Derivation of Helmholtz's reciprocity principle and Kirchhoff's law," J. Opt. Soc. Am. A **15**, 2735–2744 (1998).

[84] R. J. Potton, "Reciprocity in optics," Rep. Prog. Phys. **67**, 717–754 (2004).

[85] M. J. E. Golay, "Theoretical consideration in heat and infra-red detection, with particular reference to the pneumatic detector," Rev. Sci. Instrum. **18**, 347–356 (1947).

[86] M. J. E. Golay, "The theoretical and practical sensitivity of the pneumatic infra-red detector," Rev. Sci. Instrum. **20**, 816–820 (1949).

[87] D. Palaferri, Y. Todorov, A. Bigioli, A. Mottaghizadeh, D. Gacemi, A. Calabrese, A. Vasanelli, L. Li, A. G. Davies, E. H. Linfield, F. Kapsalidis, M. Beck, J. Faist, and C. Sirtori, "Room-temperature nine-μm-wavelength photodetectors and GHz-frequency heterodyne receivers," Nature **556**, 85–88 (2018).

[88] H. T. Miyazaki, T. Mano, T. Kasaya, H. Osato, K. Watanabe, Y. Sugimoto, T. Kawazu, Y. Arai, A. Shigetou, T. Ochiai, Y. Jimba, and H. Miyazaki, "Synchronously wired infrared antennas for resonant single-quantum-well photodetection up to room temperature," Nat. Commun. **11**, 565 (2020).

[89] H. T. Miyazaki, T. Mano, T. Noda, T. Kasaya, and Y. B. Habibullah, "Antenna-enhanced high-resistance photovoltaic infrared detectors based on quantum ratchet architecture," Appl. Phys. Lett. **124**, 231103 (2024).

[90] O. Yavas, M. Svedendahl, P. Dobosz, V. Sanz, and R. Quidant, "On-a-chip biosensing based on all-dielectric nanoresonators," Nano Lett. **17**, 4421–4426 (2017).

[91] J. Zhu, Z. Wang, S. Lin, S. Jiang, X. Liu, and S. Guo, "Low-cost flexible plasmonic nanobump metasurfaces for label-free sensing of serum tumor marker," Biosens. Bioelectron. **150**, 111905 (2020).

[92] A. Tittl, A. Leitis, M. Liu, F. Yesilkoy, D.-Y. Choi, D. N. Neshev, Y. S. Kivshar, and H. Altug, "Imaging-based molecular barcoding with pixelated dielectric metasurfaces," Science **360**, 1105–1109 (2018).

[93] M. L. Tseng, Y. Jahani, A. Leitis, and H. Altug, "Dielectric metasurfaces enabling advanced optical biosensors," ACS Photonics **8**, 47–60 (2021).

[94] J. Wang, S. A. Maier, and A. Tittl, "Trends in nanophotonics-enabled optofluidic biosensors," Adv. Opt. Mater. **10**, 2102366 (2022).

[95] S. Sun, L. Wu, Z. Geng, P. P. Shum, X. Ma, and J. Wang, "Refractometric imaging and biodetection empowered by nanophotonics," Laser Photonics Rev. **17**, 2200814 (2023).

[96] D. A. Giljohann and C. A. Mirkin, "Drivers of biodiagnostic development," Nature **462**, 461–464 (2009).

[97] A. Y. Piggott, J. Lu, K. G. Lagoudakis, J. Petykiewicz, T. M. Babinec, and J. Vučković, "Inverse design and demonstration of a compact and broadband on-chip wavelength demultiplexer," Nat. Photonics **9**, 374–377 (2015).

[98] Z. Liu, D. Zhu, S. P. Rodrigues, K.-T. Lee, and W. Cai, "Generative model for the inverse design of metasurfaces," Nano Lett. **18**, 6570–6576 (2018).

[99] A. S. Backer, "Computational inverse design for cascaded systems of metasurface optics," Opt. Express **27**, 30308–30331 (2019).

[100] M. Meem, S. Banerji, C. Pies, T. Oberbiermann, A. Majumder, B. Sensale-Rodriguez, and R. Menon, "Large-area, high-numerical-aperture multi-level diffractive lens via inverse design," Optica **7**, 252–253 (2020).

[101] J. Yang and J. A. Fan, "Topology-optimized metasurfaces: Impact of initial geometric layout," Opt. Lett. **42**, 3161–3164 (2017).

[102] T. Phan, D. Sell, E. W. Wang, S. Doshay, K. Edee, J. Yang, and J. A. Fan, "High-efficiency, large-area, topology-optimized metasurfaces," Light. Sci. Appl. **8**, 48 (2019).

[103] Z. Lin and S. G. Johnson, "Overlapping domains for topology optimization of large-area metasurfaces," Opt. Express **27**, 32445–32453 (2019).

[104] A. M. Hammond, A. Oskooi, M. Chen, Z. Lin, S. G. Johnson, and S. E. Ralph, "High-performance hybrid time/frequency-domain topology optimization for large-scale photonics inverse design," Opt. Express **30**, 4467–4491 (2022).

[105] S. Inampudi and H. Mosallaei, "Neural network based design of metagratings," Appl. Phys. Lett. **112**, 241102 (2018).

[106] J. Jiang, D. Sell, S. Hoyer, J. Hickey, J. Yang, and J. A. Fan, "Free-form diffractive metagrating design based on generative adversarial networks," ACS Nano **13**, 8872–8878 (2019).

[107] M. Iwanaga, "Optically deep asymmetric one-dimensional metallic grooves: Genetic algorithm approach," J. Opt. Soc. Am. B **26**, 1111–1118 (2009).

[108] M. Iwanaga, "Non-empirical large-scale search for optical metasurfaces," Nanomaterials **10**, 1739 (2020).

[109] M. Iwanaga, "A design strategy for surface nanostructures to realize sensitive refractive-index optical sensors," Nanomaterials **13**, 3081 (2023).

[110] S. Molesky, Z. Lin, A. Y. Piggott, W. Jin, J. Vucković, and A. W. Rodriguez, "Inverse design in nanophotonics," Nat. Photonics **12**, 659–670 (2018).

[111] K. Yao, R. Unni, and Y. Zheng, "Intelligent nanophotonics: Merging photonics and artificial intelligence at the nanoscale," Nanophotonics **8**, 339–366 (2019).

[112] S. D. Campbell, D. Sell, R. P. Jenkins, E. B. Whiting, J. A. Fan, and D. H. Werner, "Review of numerical optimization techniques for meta-device design," Opt. Mater. Express **9**, 1842–1863 (2019).

[113] Z. Li, R. Pestourie, Z. Lin, S. G. Johnson, and F. Capasso, "Empowering metasurfaces with inverse design: Principles and applications," ACS Photonics **9**, 2178–2192 (2022).

[114] L. He, Y. Li, D. Torrent, X. Zhuang, T. Rabczuk, and Y. Jin, "Machine learning assisted intelligent design meta structures: A review" Microstructures **3**, 2023037 (2023).

[115] N. Yu and F. Capasso, "Flat optics with designer metasurfaces," Nat. Mater. **13**, 139–150 (2014).

[116] S. Jahani and Z. Jacob, "All-dielectric metamaterials," Nat. Nanotechnol. **11**, 23–36 (2016).

[117] P. Genevet, F. Capasso, F. Aieta, M. Khorasaninejad, and R. Devlin, "Recent advances in planar optics: From plasmonic to dielectric metasurfaces," Optica **4**, 139–152 (2017).

[118] S. M. Kamali, E. Arbabi, A. Arbabi, and A. Faraon, "A review of dielectric optical metasurfaces for wavefront control," Nanophotonics **7**, 1041–1068 (2018).

[119] Metalenz, Inc., https://metalenz.com (last accessed December 2, 2024).

[120] Shenzhen Metalenx Technology Co., https://en.metalenx.com (last accessed December 2, 2024).

[121] J. C. Swihart, "Field solution for a thin-film superconducting strip transmission line," J. Appl. Phys. **32**, 461–469 (1961).

[122] E. N. Economou, "Surface plasmons in thin films," Phys. Rev. **182**, 539–554 (1969).

[123] H. T. Miyazaki and Y. Kurokawa, "Squeezing visible light waves into a 3-nm-thick and 55-nm-long plasmon cavity," Phys. Rev. Lett. **96**, 097401 (2006).

[124] M. Iwanaga, *Plasmonic Resonators: Fundamentals, Advances, and Applications* (Pan Stanford Publishing, Singapore, 2016).

[125] L. D. Landau, E. M. Lifshitz, and P. Pitaevskii, *Electrodynamics of Continuous Media*, 2nd ed. (Pergamon, New York, 1984).

[126] M. Iwanaga, A. S. Vengurlekar, T. Hatano, and T. Ishihara, "Reciprocal transmittances and reflectances: An elementary proof," Am. J. Phys. **75**, 899–902 (2007).

[127] J. Meng, S. Balendhran, Y. Sabri, S. K. Bhargava, and K. B. Crozier, "Smart mid-infrared metasurface microspectrometer gas sensing system," Microsyst. Nanoeng. **10**, 74 (2024).

[128] J. F. Li, Y. F. Huang, Y. Ding, Z. L. Yang, S. B. Li, X. S. Zhou, F. R. Fan, W. Zhang, Z. Y. Zhou, D. Y. Wu, B. Ren, Z. L. Wang, and Z. Q. Ti, "Shell-isolated nanoparticle-enhanced Raman spectroscopy," Nature **464**, 392–395 (2010).

[129] J. M. Lee, H. K. Park, Y. Jung, J. K. Kim, S. O. Jung, and B. H. Chung, "Direct immobilization of protein G variants with various numbers of cysteine residues on a gold surface," Anal. Chem. **79**, 2680–2687 (2007).

[130] E. A. Bruce, M.-L. Huang, G. A. Perchetti, S. Tighe, P. Laaguiby, J. J. Hoffman, D. L. Gerrard, A. K. Nalla, Y. Wei, A. L. Greninger, S. A. Diehl, D. J. Shirley, D. G. B. Leonard, C. D. Huston, B. D. Kirkpatrick, J. A. Dragon, J. W. Crothers, K. R. Jerome, and J. W. Botten, "Direct RT-QPCR detection of SARS-CoV-2 RNA from patient nasopharyngeal swabs without an RNA extraction step," PLoS Biol. **18**, e3000896 (2020).

[131] H. Yin, Z. Wu, N. Shi, Y. Qi, X. Jian, L. Zhou, Y. Tong, Z. Cheng, J. Zhao, and H. Mao, "Ultrafast multiplexed detection of SARS-CoV-2 RNA using a rapid droplet digital PCR system," Biosens. Bioelectron. **188**, 113282 (2021).

[132] M. Alafeef, K. Dighe, P. Moitra, and D. Pan, "Rapid, ultrasensitive, and quantitative detection of SARS-CoV-2 using antisense oligonucleotides directed electrochemical biosensor chip," ACS Nano **14**, 17028–17045 (2020).

[133] M. Iwanaga, "All-dielectric metasurface fluorescence biosensors for high-sensitivity antibody/antigen detection," ACS Nano **14**, 17458–17467 (2020).

[134] M. Iwanaga, "Highly sensitive wide-range target fluorescence biosensors of high-emittance metasurfaces," Biosens. Bioelectron. **190**, 113423 (2021).

[135] M. Fleischmann, P. J. Hendra, and A. J. McQuillan, "Raman spectra of pyridine adsorbed at a silver electrode," Chem. Phys. Lett. **26**, 163–166 (1974).

[136] D. L. Jeanmaire and R. P. van Duyne, "Heterocyclic, aromatic, and aliphatic amines adsorbed on the anodized silver electrode," J. Electroanal. Chem. Interf. Electrochem. **84**, 1–20 (1977).

[137] M. G. Albrecht and J. A. Creighton, "Anomalously intense Raman spectra of pyridine at a silver electrode," J. Am. Chem. Soc. **99**, 5215–5217 (1977).

[138] P. F. Liao and M. B. Stern, "Surface-enhanced Raman scattering on gold and aluminum particle arrays," Opt. Lett. **7**, 483–485 (1982).

[139] S. Nie and S. R. Emory, "Probing single molecules and single nanoparticles by surface-enhanced Raman scattering," Science **275**, 1102–1106 (1997).

[140] K. Kneipp, Y. Wang, H. Kneipp, L. T. Perelman, I. Itzkan, R. R. Dasari, and M. S. Feld, "Single molecule detection using surface-enhanced Raman scattering (SERS)," Phys. Rev. Lett. **78**, 1667–1670 (1997).

[141] C. M. Galloway, P. G. Etchegoin, and E. C. Le Ru, "Ultrafast nonradiative decay rates on metallic surfaces by comparing surface-enhanced Raman and fluorescence signals of single molecules," Phys. Rev. Lett. **103**, 063003 (2009).

[142] W.-D. Li, F. Ding, J. Hu, and S. Y. Chou, "Three-dimensional cavity nanoantenna coupled plasmonic nanodots for ultrahigh and uniform surface-enhanced Raman scattering over large area," Opt. Express **19**, 3925–3936 (2011).

[143] S. Shen, J. Wang, Y. Zhu, W. Yang, R. Gao, J.-F. Li, G. Sun, and Y. Zhilin, "Large-area metal-dielectric heterostructures for surface-enhanced raman scattering," Opt. Express **30**, 38256–38265 (2022).

[144] J. Langer, D. Jimenez de Aberasturi, J. Aizpurua, R. A. Alvarez-Puebla, B. Auguié, J. J. Baumberg, G. C. Bazan, S. E. J. Bell, A. Boisen, A. G. Brolo, J. Choo, D. Cialla-May, V. Deckert, L. Fabris, K. Faulds, F. J. García de Abajo, R. Goodacre, D. Graham, A. J. Haes, C. L. Haynes, C. Huck, T. Itoh, M. Käll, J. Kneipp, N. A. Kotov, H. Kuang, E. C. Le Ru, H. K. Lee, J.-F. Li, X. Y. Ling, S. A. Maier, T. Mayerhöfer, M. Moskovits, K. Murakoshi, J.-M. Nam, S. Nie, Y. Ozaki, I. Pastoriza-Santos, J. Perez-Juste, J. Popp, A. Pucci, S. Reich, B. Ren, G. C. Schatz, T. Shegai, S. Schlücker, L.-L. Tay, K. G. Thomas, Z.-Q. Tian, R. P. Van Duyne, T. Vo-Dinh, Y. Wang, K. A. Willets, C. Xu, H. Xu, Y. Xu, Y. S. Yamamoto, B. Zhao, and L. M. Liz-Marzán, "Present and future of surface-enhanced Raman scattering," *ACS Nano* **14**, 28–117 (2020).

[145] H. Raether, *Surface Plasmons on Smooth and Rough Surfaces and on Gratings* (Springer-Verlag, Berlin, 1988).

[146] D. G. Myszka, X. He, M. Dembo, T. A. Morton, and B. Goldstein, "Extending the range of rate constants available from BIACORE: Interpreting mass transport-influenced binding data," Biophys. J. **75**, 583–594 (1998).

[147] G. K. Joshi, S. Deitz-McElyea, T. Liyanage, K. Lawrence, S. Mali, R. Sardar, and M. Korc, "Label-free nanoplasmonic-based short noncoding RNA sensing at attomolar concentrations allows for quantitative and highly specific assay of microrna-10b in biological fluids and circulating exosomes," ACS Nano **9**, 11075–11089 (2015).

[148] A. E. Cetin, D. Etezadi, B. C. Galarreta, M. P. Busson, Y. Eksioglu, and H. Altug, "Plasmonic nanohole arrays on a robust hybrid substrate for highly sensitive label-free biosensing," ACS Photonics **2**, 1167–1174 (2015).

[149] J. Zhou, F. Tao, J. Zhu, S. Lin, Z. Wang, X. Wang, J.-Y. Ou, Y. Li, and Q. H. Liu, "Portable tumor biosensing of serum by plasmonic biochips in combination with nanoimprint and microfluid," Nanophotonics **8**, 307–316 (2019).

[150] A. Miti, S. Thamm, P. Muller, A. Csaki, W. Fritzsche, and G. Zuccheri, "A miRNA biosensor based on localized surface plasmon resonance enhanced by surface-bound hybridization chain reaction," Biosens. Bioelectron. **167**, 112465 (2020).

[151] B. Bagra, T. Mabe, F. Tukur, and J. Wei, "A plasmonic nanoledge array sensor for detection of anti-insulin antibodies of type 1 diabetes biomarker," Nanotechnology **31**, 325503 (2020).

[152] Y. Jahani, E. R. Arvelo, F. Yesilkoy, K. Koshelev, C. Cianciaruso, M. D. Palma, Y. Kivshar, and H. Altug, "Imaging-based spectrometer-less optofluidic biosensors based on dielectric metasurfaces for detecting extracellular vesicles," Nat. Commun. **12**, 3246 (2021).

[153] L. Tang and J. Li, "Plasmon-based colorimetric nanosensors for ultrasensitive molecular diagnostics," ACS Sens. **2**, 857–875 (2017).

[154] Y. Zhang, D. Wang, S. Yue, Y. Lu, C. Yang, J. Fang, and Z. Xu, "Sensitive multicolor visual detection of exosomes via dual signal amplification strategy of enzyme-catalyzed metallization of au nanorods and hybridization chain reaction," ACS Sens. **4**, 3210–3218 (2019).

[155] F. Neubrech, A. Pucci, T. W. Cornelius, S. Karim, A. García-Etxarri, and J. Aizpurua, "Resonant plasmonic and vibrational coupling in a tailored nanoantenna for infrared detection," Phys. Rev. Lett. **101**, 157403 (2008).

[156] R. Adato, A. A. Yanik, J. J. Amsden, D. L. Kaplan, F. G. Omenetto, M. K. Hong, S. Erramilli, and H. Altug, "Ultra-sensitive vibrational spectroscopy of protein monolayers with plasmonic nanoantenna arrays," Proc. Natl. Acad. Sci. U. S. A. **106**, 19227–19232 (2009).

[157] U. Fano, "Effects of configuration interaction on intensities and phase shifts," Phys. Rev. **124**, 1866–1878 (1961).

[158] A. E. Miroshnichenko, S. Flach, and Y. S. Kivshar, "Fano resonances in nanoscale structures," Rev. Mod. Phys. **82**, 2257–2298 (2010).

[159] O. Selig, R. Siffels, and Y. L. A. Rezus, "Ultrasensitive ultrafast vibrational spectroscopy employing the near field of gold nanoantennas," Phys. Rev. Lett. **114**, 233004 (2015).

[160] T. H. H. Le and T. Tanaka, "Plasmonics–nanofluidics hydrid metamaterial: An ultrasensitive platform for infrared absorption spectroscopy and quantitative measurement of molecules," ACS Nano **11**, 9780–9788 (2017).

[161] D.-S. Su, D. P. Tsai, T.-J. Yen, and T. Tanaka, "Ultrasensitive and selective gas sensor based on a channel plasmonic structure with an enormous hot spot region," ACS Sens. **4**, 2900–2907 (2019).

[162] J. Xu, Z. Ren, B. Dong, X. Liu, C. Wang, Y. Tian, and C. Lee, "Nanometer-scale heterogeneous interfacial sapphire wafer bonding for enabling plasmonic-enhanced nanofluidic mid-infrared spectroscopy," ACS Nano **14**, 12159–12172 (2020).

[163] Z. Ren, Z. Zhang, J. Wei, B. Dong, and C. Lee, "Wavelength-multiplexed hook nanoantennas for machine learning enabled mid-infrared spectroscopy," Nat. Commun. **13**, 3859 (2022).

[164] K. Watanabe, H. R. Devi, M. Iwanaga, and T. Nagao, "Vibrational coupling to quasi-bound states in the continuum under tailored coupling conditions," Adv. Opt. Mater. **12**, 2301912 (2024).

[165] Human CEA ELISA Kit, ab264604, https://www.abcam.com/products/elisa-kits/human-cea-elisa-kit-ab264604.html (last accessed December 2, 2024).

[166] D. M. Rissin, C. W. Kan, T. G. Campbell, S. C. Howes, D. R. Fournier, L. Song, T. Piech, P. P. Patel, L. Chang, A. J. Rivnak, E. P. Ferrell, J. D. Randall, G. K. Provuncher, D. R. Walt, and D. C. Duffy, "Single-molecule enzyme-linked immunosorbent assay detects serum proteins at subfemtomolar concentrations," Nat. Biotechnol. **28**, 595–599 (2010).

[167] S. H. Kim, S. Iwai, S. Araki, S. Sakakihara, R. Iino, and H. Noji, "Large-scale femtoliter droplet array for digital counting of single biomolecules," Lab Chip **12**, 4986–4991 (2012).

[168] R. K. Saiki, N. Arnheim, and H. A. Erlich, "A novel method for the detection of polymorphic restriction sites by cleavage of oligonucleotide probes: Application to sickle-cell anemia," Nat. Biotechnol. **3**, 1008–1012 (1985).

[169] R. K. Saiki, S. Scharf, F. Faloona, K. B. Mullis, G. T. Horn, H. A. Erlich, and N. Arnheim, "Enzymatic amplification of β-globin genomic sequences and restriction site analysis for diagnosis of sickle cell anemia," Science **230**, 1350–1354 (1985).

[170] B. Udugama, P. Kadhiresan, H. N. Kozlowski, A. Malekjahani, M. Osborne, V. Y. C. Li, H. Chen, S. Mubareka, J. B. Gubbay, and W. C. W. Chan, "Diagnosing COVID-19: The disease and tools for detection," ACS Nano **14**, 3822–3835 (2020).

[171] T. Ji, Z. Liu, G. Wang, X. Guo, S. A. Khan, C. Lai, H. Chen, S. Huang, S. Xia, B. Chen, H. Jia, Y. Chen, and Q. Zhou, "Detection of COVID-19: A review of the current literature and future perspectives," Biosens. Bioelectron. **166**, 112455 (2020).

[172] Y. Y. Zuo, W. E. Uspal, and T. Wei, "Airborne transmission of COVID-19: Aerosol dispersion, lung deposition, and virus-receptor interactions," ACS Nano **14**, 16502–16524 (2020).

[173] E. Noviana, T. Ozer, C. S. Carrell, J. S. Link, C. McMahon, I. Jang, and C. S. Henry, "Microfluidic paper-based analytical devices: From design to applications," Chem. Rev. **121**, 11835–11885 (2021).

[174] M. Xiao, F. Tian, X. Liu, Q. Zhou, J. Pan, Z. Luo, M. Yang, and C. Yi, "Virus detection: From state-of-the-art laboratories to smartphone-based point-of-care testing," Adv. Sci. **9**, 2105904 (2022).

[175] M. Alafeef and D. Pan, "Diagnostic approaches for COVID-19: Lessons learned and the path forward," ACS Nano **16**, 11545–11576 (2022).

[176] P. J. Sykes, S. H. Neoh, M. J. Brisco, E. Hughes, J. Condon, and A. A. Morley, "Quantitation of targets for PCR by use of limiting dilution," Biotechniques **13**, 444–449 (1992).

[177] O. Kalinina, I. Lebedeva, J. Brown, and J. Silver, "Nanoliter scale PCR with TaqMan detection," Nucl. Acids Res. **25**, 1999–2004 (1997).

[178] B. Vogelstein and K. W. Kinzler, "Digital PCR," Proc. Natl. Acad. Sci. U. S. A. **96**, 9236–9241 (1999).

[179] J. Baranwal, B. Barse, G. Gatto, G. Broncova, and A. Kumar, "Electrochemical sensors and their applications: A review," Chemosensors **10**, 363 (2022).

[180] K. Akama, K. Shirai, and S. Suzuki, "Droplet-free digital enzyme-linked immunosorbent assay based on a tyramide signal amplification system," Anal. Chem. **88**, 7123–7129 (2016).

[181] K. Akama, N. Iwanaga, K. Yamawaki, M. Okuda, K. Jain, H. Ueno, N. Soga, Y. Minagawa, and H. Noji, "Wash- and amplification-free digital immunoassay based on single-particle motion analysis," ACS Nano **13**, 13116–13126 (2019).

[182] H. Shu, W. Wen, H. Xiong, X. Zhang, and S. Wang, "Novel electrochemical aptamer biosensor based on gold nanoparticles signal amplification for the detection of carcinoembryonic antigen," Electrochem. Commun. **37**, 15–19 (2013).

[183] J. Zhou, L. Du, L. Zou, Y. Zou, N. Hu, and P. Wang, "An ultrasensitive electrochemical immunosensor for carcinoembryonic antigen detection based on staphylococcal protein A–Au nanoparticle modified gold electrode," Sens. Actuat. B: Chem. **197**, 220–227 (2014).

[184] X. Wang, C. Chu, L. Shen, W. Deng, M. Yan, S. Ge, J. Yu, and X. Song, "An ultrasensitive electrochemical immunosensor based on the catalytical activity of MoS_2-Au composite using Ag nanospheres as labels," Sens. Actuat. B: Chem. **206**, 30–36 (2015).

[185] X. Li, M. Yu, Z. Chen, X. Lin, and Q. Wu, "A sensor for detection of carcinoembryonic antigen based on the polyaniline-Au nanoparticles and gap-based interdigitated electrode," Sens. Actuat. B: Chem. **239**, 874–882 (2017).

[186] P. Miao, Y. Jiang, Y. Wang, J. Yin, and Y. Tang, "An electrochemical approach capable of prostate specific antigen assay in human serum based on exonuclease-aided target recycling amplification," Sens. Actuat. B: Chem. **257**, 1021–1026 (2018).

[187] M. Iwanaga, "All-dielectric metasurfaces with high-fluorescence-enhancing capability," Appl. Sci. **8**, 1328 (2018).

[188] B. Choi, M. Iwanaga, H. T. Miyazaki, Y. Sugimoto, A. Ohtake, and K. Sakoda, "Overcoming metal-induced fluorescence quenching on plasmo-photonic metasurfaces coated by a self-assembled monolayer," Chem. Commun. **51**, 11470–11473 (2015).

[189] M. Iwanaga, B. Choi, H. T. Miyazaki, and Y. Sugimoto, "The artificial control of enhanced optical processes in fluorescent molecules on high-emittance metasurfaces," Nanoscale **8**, 11099–11107 (2016).

[190] J. Breault-Turcot, H.-P. Poirier-Richard, M. Couture, D. Pelechacz, and J.-F. Masson, "Single chip SPR and fluorescent ELISA assay of prostate specific antigen," Lab Chip **15**, 4433–4440 (2015).

[191] Y. Wang, M. A. Ali, E. K. Chow, L. Dong, and M. Lu, "An optofluidic metasurface for lateral flow-through detection of breast cancer biomarker," Biosens. Bioelectron. **107**, 224–229 (2018).

[192] M. Iwanaga, "High-sensitivity high-throughput detection of nucleic-acid targets on metasurface fluorescence biosensors," Biosensors **11**, 33 (2021).

[193] J. Qin, S. Jiang, Z. Wang, X. Cheng, B. Li, Y. Shi, D. P. Tsai, A. Q. Liu, W. Huang, and W. Zhu, "Metasurface micro/nano-optical sensors: Principles and applications," ACS Nano **16**, 11598–11618 (2022).

[194] A. Kinkhabwala, Z. Yu, S. Fan, Y. Avlasevich, K. Müllen, and W. E. Moerner, "Large single-molecule fluorescence enhancements produced by a bowtie nanoantenna," Nat. Photonics **3**, 654–657 (2009).

[195] M. Schmelzeisen, Y. Zhao, M. Klapper, K. Müllen, and M. Kreiter, "Fluorescence enhancement from individual plasmonic gap resonances," ACS Nano **4**, 3309–3317 (2010).

[196] C.-C. Fu, G. Ossato, M. Long, M. A. Digman, A. Gopinathan, L. P. Lee, E. Gratton, and M. Khine, "Bimetallic nanopetals for thousand-fold fluorescence enhancements," Appl. Phys. Lett. **97**, 203101 (2010).

[197] W. Zhang, F. Ding, W.-D. Li, Y. Wang, J. Hu, and S. Y. Chou, "Giant and uniform fluorescence enhancement over large areas using plasmonic nanodots in 3D resonant cavity nanoantenna by nanoimprinting," Nanotechnology **23**, 225301 (2012).

[198] L. Zhou, F. Ding, H. Chen, W. Ding, W. Zhang, and S. Y. Chou, "Enhancement of immunoassay's fluorescence and detection sensitivity using three-dimensional plasmonic nano-antenna-dots array," Anal. Chem. **84**, 4489–4495 (2012).

[199] D. Punj, M. Mivelle, S. B. Moparthi, T. S. van Zanten, H. Rigneault, N. F. van Hulst, M. F. García-Parajó, and J. Wenger, "A plasmonic 'antenna-in-box' platform for enhanced single-molecule analysis at micromolar concentrations," Nat. Nanotechnol. **8**, 512–516 (2013).

[200] Z. Dong, S. Gorelik, R. Paniagua-Dominguez, J. Yik, J. Ho, F. Tjiptoharsono, E. Lassalle, S. D. Rezaei, D. C. J. Neo, P. Bai, A. I. Kuznetsov, and J. K. W. Yang, "Silicon nanoantenna mix arrays for a trifecta of quantum emitter enhancements," Nano Lett. **21**, 4853–4860 (2021).

[201] M. Iwanaga, B. Choi, H. T. Miyazaki, Y. Sugimoto, and K. Sakoda, "Large-area resonance-tuned metasurfaces for on-demand enhanced spectroscopy," J. Nanomater **2015**, 507656.

[202] S. Sederberg and A. Elezzabi, "Sierpiński fractal plasmonic antenna: A fractal abstraction of the plasmonic bowtie antenna," Opt. Express **19**, 10456–10461 (2011).

[203] A. M. Glass, P. F. Liao, J. G. Bergman, and D. H. Olson, "Interaction of metal particles with adsorbed dye molecules: Absorption and luminescence," Opt. Lett. **5**, 368–370 (1980).

[204] J. R. Lakowicz, K. Ray, M. Chowdhury, H. Szmacinski, Y. Fu, J. Zhang, and K. Nowaczyk, "Plasmon-controlled fluorescence: A new paradigm in fluorescence spectroscopy," Analyst **133**, 1308–1348 (2008).

[205] M. Bauch, K. Toma, M. Toma, Q. Zhang, and J. Dostalek, "Plasmon-enhanced fluorescence biosensors: A review," Plasmonics **9**, 781–799 (2014).

[206] M. Iwanaga and B. Choi, "Heteroplasmon hybridization in stacked complementary plasmo–photonic crystals," Nano Lett. **15**, 1904–1910 (2015).

[207] B. Choi, M. Iwanaga, H. T. Miyazaki, K. Sakoda, and Y. Sugimoto, "Photoluminescence-enhanced plasmonic substrates fabricated by nanoimprint lithography," J. Micro/Nanolith. MEMS MOEMS **13**, 023007 (2014).

[208] A. F. Koenderink, "Single-photon nanoantennas," ACS Photonics **4**, 710–722 (2017).

[209] E. M. Purcell, "Spontaneous emission probabilities at radio frequencies," Phys. Rev. **69**, 681 (1946).

[210] P. Anger, P. Bharadwaj, and L. Novotny, "Enhancement and quenching of single-molecule fluorescence," Phys. Rev. Lett. **96**, 113002 (2006).

[211] R. R. Chance, A. Prock, and R. Silbey, "Molecular fluorescence and energy transfer near interfaces," Adv. Chem. Phys. **37**, 1–65 (1978).

[212] M. Iwanaga, X. Yang, V. Karanikolas, T. Kuroda, and Y. Sakuma, "2D-material-fused high-emittance plasmo–photonic metasurfaces," Adv. Opt. Mater. **12**, 2303309 (2024).

[213] M. Iwanaga, X. Yang, V. Karanikolas, T. Kuroda, and Y. Sakuma, "Prominently enhanced luminescence from a continuous monolayer of transition metal dichalcogenide on all-dielectric metasurfaces," Nanophotonics **13**, 95–105 (2024).

[214] M. Iwanaga and W. Tangkawsakul, "Two-way detection of COVID-19 spike protein and antibody using all-dielectric metasurface fluorescence sensors," Biosensors **12**, 981 (2022).

[215] M. Iwanaga, "Rapid detection of attomolar SARS-CoV-2 nucleic acids in all-dielectric metasurface biosensors," Biosensors **12**, 987 (2022).

[216] R. R. Neubig, M. Spedding, T. Kenakin, and A. Christopoulos, "International union of pharmacology committee on receptor nomenclature and drug classification. XXXVIII. Update on terms and symbols in quantitative pharmacology," Pharmacol. Rev. **55**, 597–606 (2003).

[217] R. Gesztelyi, J. Zsuga, A. Kemeny-Beke, B. Varga, B. Juhasz, and A. Tosaki, "The Hill equation and the origin of quantitative pharmacology," Arch. Hist. Exact Sci. **66**, 427–438 (2012).

[218] Q. Hu, M. Iwanaga, and Y. Tang, "Metasurface platform incorporating aggregation induced emission based biosensor for enhanced human serum albumin detection," Adv. Opt. Mater. **12**, 2400868 (2024).

[219] H. Ochiai, T. Ohishi, K. Osumi, J. Tokuyama, H. Urakami, S. Seki, A. Shimada, A. Matsui, Y. Isobe, Y. Murata, T. Endo, Y. Ishii, H. Hasegawa, S. Matsumoto, and Y. Kitagawa, "Reevaluation of serum p53 antibody as a tumor marker in colorectal cancer patients," Surg. Today **42**, 164–168 (2012).

[220] K. Kumamoto, H. Ishida, K. Kuwabara, K. Amano, N. Chika, N. Okada, T. Ohsawa, Y. Kumagai, and K. Ishibashi, "Clinical significance of serum anti-p53 antibody expression following curative surgery for colorectal cancer," Mol. Clin. Oncol. **7**, 595–600 (2017).

[221] S. Liu, Q. Tan, Y. Song, Y. Shi, and X. Han, "Anti-p53 autoantibody in blood as a diagnostic biomarker for colorectal cancer: A meta-analysis," Scand. J. Immunol. **91**, e12829 (2020).

[222] S. Cristiano, A. Leal, J. Phallen, J. Fiksel, V. Adleff, D. C. Bruhm, S. Ø. Jensen, J. E. Medina, C. Hruban, J. R. White, D. N. Palsgrove, N. Niknafs, V. Anagnostou, P. Forde, J. Naidoo, K. Marrone, J. Brahmer, B. D. Woodward, H. Husain, K. L. van Rooijen, M.-B. W. Ørntoft, A. H. Madsen, C. J. H. van de Velde, M. Verheij, A. Cats, C. J. A. Punt, G. R. Vink, N. C. T. van Grieken, M. Koopman, R. J. A. Fijneman, J. S. Johansen, H. J. Nielsen, G. A. Meijer, C. L. Andersen, R. B. Scharpf, and V. E. Velculescu, "Genome-wide cell-free DNA fragmentation in patients with cancer," Nature **570**, 385–389 (2019).

[223] Y. M. D. Lo, D. S. C. Han, P. Jiang, and R. W. K. Chiu, "Epigenetics, fragmentomics, and topology of cell-free DNA in liquid biopsies," Science **372**, eaaw3616 (2021).

[224] T. Sugasawa, S. Fujita, T. Kuji, N. Ishibashi, K. Tamai, Y. Kawakami, and K. Takekoshi, "Dynamics of specific cfDNA fragments in the plasma of full marathon participants," Genes **12**, 676 (2021).

[225] LOD of SARS-CoV-2 by RT-PCR. https://www.niid.go.jp/niid/ja/covid-19/9482-covid14-15.html (in Japanese) (last accessed December 9, 2024).

[226] Z. Zhang, Z. Deng, L. Zhu, J. Zeng, X. M. Cai, Z. Qiu, Z. Zhao, and B. Tang, "Aggregation-induced emission biomaterials for anti-pathogen medical applications: Detecting, imaging and killing," Regen. Biomater. **10**, rbad044 (2023).

[227] Y. Hong, J. W. Y. Lam, and B. Tang, "Aggregation-induced emission," Chem. Soc. Rev. **40**, 5361–5388 (2011).

[228] Y. Hong, J. W. Y. Lam, and B. Tang, "Aggregation-induced emission: Phenomenon, mechanism and applications," Chem. Commun. **2009**, 4332–4353 (2009).

[229] Y. Chen, J. W. Y. Lam, R. T. K. Kwok, B. Liu, and B. Tang, "Aggregation-induced emission: Fundamental understanding and future developments," Mater. Horiz. **6**, 428–433 (2019).

[230] J. Mei, N. L. C. Leung, R. T. K. Kwok, J. W. Y. Lam, and B. Tang, "Aggregation-induced emission: Together we shine, united we soar!," Chem. Rev. **115**, 11718–11940 (2015).

[231] S. Xu, Y. Duan, and B. Liu, "Precise molecular design for high–performance luminogens with aggregation–induced emission," Adv. Mater. **32**, 1903530 (2020).

[232] J. Mei, Y. Hong, J. W. Y. Lam, A. Qin, Y. Tang, and B. Tang, "Aggregation–induced emission: The whole is more brilliant than the parts," Adv. Mater. **26**, 5429–5479 (2014).

[233] W. Wu and B. Liu, "Aggregation-induced emission: Challenges and opportunities," Natl. Sci. Rev. **8**, nwaa222 (2021).

[234] D. Wang and B. Tang, "Aggregation-induced emission luminogens for activity-based sensing," Acc. Chem. Res. **52**, 2559–2570 (2019).

[235] X. Cai and B. Liu, "Aggregation-induced emission: Recent advances in materials and biomedical applications," Angew. Chem. Int. Ed. **59**, 9868–9886 (2020).

[236] H. Wang and G. Liu, "Advances in luminescent materials with aggregation-induced emission (AIE) properties for biomedical applications," J. Mater. Chem. B **6**, 4029–4042 (2018).

[237] R. T. K. Kwok, C. W. T. Leung, J. W. Y. Lam, and B. Tang, "Biosensing by luminogens with aggregation-induced emission characteristics," Chem. Soc. Rev. **44**, 4228–4238 (2015).

[238] Y. Hong, C. Feng, Y. Yu, J. Liu, J. W. Y. Lam, K. Q. Luo, and B. Tang, "Quantitation, visualization, and monitoring of conformational transitions of human serum albumin by a tetraphenylethene derivative with aggregation-induced emission characteristics," Anal. Chem. **82**, 7035–7043 (2010).

[239] R. Hu, J. Wang, A. Qin, and B. Tang, "Aggregation-induced emission-active biomacromolecules: Progress, challenges, and opportunities," Biomacromolecules **23**, 2185–2196 (2022).

[240] A. Irrera, A. A. Leonardi, C. Di Franco, M. J. Lo Faro, G. Palazzo, C. D'Andrea, K. Manoli, G. Franzò, P. Musumeci, B. Fazio, L. Torsi, and F. Priolo, "New generation of ultrasensitive label-free optical Si nanowire-based biosensors," ACS Photonics **5**, 471–479 (2018).

[241] Y. Tu, Y. Yu, Z. Zhou, S. Xie, B. Yao, S. Guan, B. Situ, Y. Liu, R. T. K. Kwok, J. W. Y. Lam, S. Chen, X. Huang, Z. Zeng, and B. Tang, "Specific and quantitative detection of albumin in biological fluids by tetrazolate-functionalized water-soluble AIEgens," ACS Appl. Mater. Interfaces **11**, 29619–29629 (2019).

[242] M. Iwanaga, "Productive biosensing techniques empowered by all-dielectric metasurfaces," Front. Bioeng. Biotechnol. **12**, 1484638 (2025).

[243] The Nobel Prize in Chemistry (2024). https://www.nobelprize.org/prizes/chemistry/2024/summary/ (last accessed February 13, 2025).